THEORETICAL PREDICTION AND STUDIES OF SELECTED NOVEL MATERIALS UNDER AMBIENT AND EXTREME CONDITIONS

A Thesis submitted to the

College of Graduate and Postdoctoral Studies

In Partial fulfilment of the requirements for the Degree of Master of Science

In the Department of Physics and Engineering Physics

University of Saskatchewan

Saskatoon

By

ADEBAYO ABAYOMI ADELEKE

PERMISSION TO USE

In presenting this thesis in partial fulfilment of the requirements for a Postgraduate degree from the University of Saskatchewan, I agree that the libraries of this University may make it freely available for inspection. I further agree that permission for copying of this thesis in any manner, in whole or in part, for scholarly purpose may be granted by the professor or professors who supervised my thesis work or, in their absence, by the Head of the Department or the Dean of the college in which my thesis work was done. It is understood that any copying or publication or use of this thesis or parts thereof for financial gain shall not be allowed without any written permission. It is also understood that due recognition shall be given to me and to the University of Saskatchewan in any scholarly use which may be made of any material in my thesis.

Requests for permission to copy or make other use of material in the thesis in whole or part should be addressed to:

Head of the Department of Physics and Engineering Physics

116 Science Place

University of Saskatchewan

Saskatoon, Saskatchewan

S7N 5E2 Canada.

OR

The Dean
College of Graduate and Postdoctoral Studies
University of Saskatchewan
107 Administration Place
Saskatoon, Saskatchewan S7N 5A2
Canada.

ABSTRACT

The development of powerful computer algorithms that are specialized at exploring the energy landscape of chemical systems has revolutionized chemical physics and its derived disciplines. Such algorithms that ranges from random search to genetic algorithm are capable of uncovering a geometric configuration for a combination of chemical elements with minimum energy. The unbiased particle swarm-intelligence optimization algorithm extends the capabilities of the genetic algorithm by incorporating social intelligence through particle communication. Social communication during energy surface exploration improves the efficiency and convergence of the algorithm by preventing prediction of similar-energy structures. Particle swarm-intelligence optimization algorithm is capable of solving crystal structure problems and predicting novel crystal structures across dimensions ranging from 0D (clusters) to 3D bulk solids at specific pressure. In this study, the particle swarm-intelligence optimization algorithm was used to study and solve crystal structure problems relating to two classes of materials of industrial significance – high energy density materials and bimetallic nanoclusters.

As a significant step towards solving the problem of finding a single-bonded allotrope of nitrogen, we discuss the prediction and characterization of this member of very important class of material – high energy density materials (HEDMs). A new allotrope of nitrogen formed solely by N−N single bonds is predicted to exist between 100 and 150 GPa using the metadynamics algorithm with a biased potential. The crystal structure is characterized by a distorted tetrahedral network consisting of fused N_8, N_{10}, and N_{12} rings. Stability of the structure is established by

phonon and vibrational free energy calculations at zero and finite temperatures, respectively. The simulated x-ray diffraction pattern of the new phase is compared to the pattern of a recently synthesized nitrogen phase at the same *P-T* conditions and an excellent agreement is observed. This suggests the new phase is likely to form above the stability field of cubic gauche (cg) phase. The outstanding metastability of the new phase is attributed to the intrinsic stability of the sp^3 bonding as well as the energetically favorable dihedral angles between N−N single bonds, in either *gauche* or *trans* conformation. The results of this work after the lab-synthesized cg phase will stimulate new research on metastable phases of nitrogen and their applications as environment-friendly HEDMs.

Furthermore, in the second part of this thesis, bimetallic cluster growth is theoretically explored up to the bulk phase. Small clusters provide a unique medium between a single atom and the bulk crystal. Preliminary theoretical and experimental results show that the geometric structures and electronic properties of clusters often differ radically from those of the solid state. Here, a first-principles investigation to explore the growth mechanism of bimetallic clusters Al_nAu_n (n=1-10) and AlAu crystal structures is carried out. It was found that the tetrahedral Al_2Au_2 cluster can serve as the building block to construct the subsequent nanomaterials as a function of the cluster size until the AlAu bulk. The results in this work provide a clear illustration of how structure evolve from a two-atom particle to multi-atom nanoclusters, and to 3D bulk element. Continued experimental and theoretical studies of these Al_nAu_n clusters may lead to the discovery of how properties transform from a particle to the bulk phase which has important technological implications in electronics, engineering and catalysis.

STATEMENT OF CO-AUTHORSHIP

The research in this thesis are a result of collaborations between the author, Adebayo A. Adeleke, supervisor Dr. Yansun Yao of the Department of Physics and Engineering Physics at the University of Saskatchewan, Biao Wan and Dr. Huiyang Gou of Center for High Pressure Science and Technology Advanced Research, Beijing 100094, China and Key Laboratory of Applied Chemistry, College of Environmental and Chemical Engineering, Yanshan University, Qinhuangdao 066004, China, Dr. Xiao Wang and Dr. Meng Zhang of the Department of Physics, East China University of Science and Technology, Shanghai 200237, China whose contributions are described below.

Chapter 1 described the underlying theory and computational tools employed in this thesis, and was written by Adebayo Abayomi Adeleke.

Chapter 2 is based on the paper 'a new single-bonded high-pressure allotrope of nitrogen' accepted for publication in Physical Review B. Calculation of equations of state and phonon dispersion were carried out by Adebayo Abayomi Adeleke. Analysis of thermodynamic stability of candidate structures at different *P-T* conditions were performed by Adebayo Abayomi Adeleke and Dr. Yansun Yao. Crystal structure prediction was carried out by Dr. Yansun Yao. COHP and the ICOHP values for bonded N-N pairs in cg and *Pccn* structures were performed by Biao Wan and Dr. Huiyang Gou. Analysis and manuscript drafting were performed by all authors.

Chapter 3 is based on the paper 'Growth Mechanism of Bimetallic Nanoalloy Clusters: Al_nAu_n (n=1-10)' by Xiao Wang, Adebayo A. Adeleke, Wei Cao, Youhua Luo, Meng Zhang, and Yansun Yao [J. Phys. Chem. C, **2016**, 120(44), 25588-25595]. Calculation of electronic

dispersion, phonon dispersion and Bader charge analysis for the bulk $P2_1/m$ phase were carried out by Adebayo A. Adeleke. Structure prediction, the deformation electron density (DED) of the Al_4Au_4 and Al_5Au_5 clusters and relative potential energy (eV) of the Al_4Au_4 and Al_5Au_5 clusters and Al-Au bulk for the lowest-energy structures and molecular dynamics simulation were carried out by Dr, Xiao Wang, Dr. Wei Cao, Dr. Youhua Luo, Dr. Meng Zhang and Dr. Yansun Yao. Manuscript was drafted by all authors.

A few other studies have been performed, but not included in this thesis for reasons of continuity. The manuscripts resulted from these studies are all in the review or preparation stage,

(1) A. A. Adeleke, E. Jossou and Y. Yao, Stable BaCl solid at high pressure: Prediction and characterization using first principles approach, J. App. Phys. (Accepted).

(2) A. A. Adeleke and Y. Yao, B1-B2 phase transition mechanism and pathway of PbS under pressure, J. Chem. Phys. (under review).

(3) L. Yang, J. Zhu, A. A. Adeleke, Y. Yao, D. Zhang, M. Jin, Y. Wang, B. Li, J. Shu, G. Shen, W. Yang, C. Jin, H.-k. Mao, Cold Compressed Graphite: A Collapsed Carbon Phase, (in preparation).

ACKNOWLEDGEMENT

Three times I pleaded with the Lord about this, that it should leave me. But He said to me, "My **grace** is sufficient for you, for my power is made perfect in weakness." Therefore, I will boast all the more gladly of my weaknesses, so that the power of Christ may rest upon me (2 Corinthians 12:8-9). I return all glory to God of all for the grace to start and finish strong.

I gratefully acknowledge the supportive, fatherly and mentor role played by my supervisor, Dr. Yansun Yao. Thank you sir for believing in me even when I failed myself. I also appreciate the patience and supportive role of my advisory committee members: Dr. Adam Bourassa, Dr. Kaori Tanaka and Dr. John S. Tse. Special thanks to all my instructors in the cause of my MSc program – Dr. John S. Tse, Dr. Rainer Dick and Dr. Masoud Ghezelbash. Thank you Debbie Gjertsen and Marjorie Granrude for assisting with all paper and administrative works and making my stay in the department memorable. To the rest of the high pressure physics group members, past and present – Dr. Xue Yong, Arnab Majumdar, Michael Greschner, Dr. Ketao Yin and Mensah David, thank you all.

Lastly, I acknowledge access to high-performance supercomputers, Compute Canada (Westgrid), and Plato at the University of Saskatchewan. I also gratefully acknowledge the financial support of Canadian Natural Sciences and Engineering Research Council (NSERC) and the Department of Physics and Engineering Physics. A big thank you to the African Institute for Mathematical Sciences (AIMS) for financial support in the form of travel grant through post AIMS bursary which open way for all the good experiences I had during my study at the University of Saskatchewan.

تفان

To my family and the memory of my beloved late sister.

TABLE OF CONTENTS

page

LIST OF TABLES

LIST OF FIGURES

Figure page

LIST OF ABBREVIATIONS

0D …… Zero dimension

1D …… One dimension

2D …… Two dimension

3D …… Three dimension

B88 …… Becke

BP …… Black phosphorus

BZ …… Brillouin zone

CALYPSO …… Crystal structure AnaLYsis by Particle Swarm Optimization

CASTEP …… Cambridge Serial Total Energy Package

Cg …… Cubic Gauche

COHP …… Crystal-orbital Hamilton-population

DED …… Deformation electron density

DFPT …… Density functional perturbation theory

DFT …… Density functional theory

EM …… Energetic materials

EOS …… equations of state

FC …….……. Force constant

GGA …….……. Generalized-gradient approximations

GPa …….……. GigaPasca

HEDM …….……...……. High-energy-density material

HK …….…….……...……. Hohenberg-Kohn

HOMO …….……. Highest occupied molecular orbital

ICOHP …….……...…. Integrated crystal-orbital Hamilton population

IFC …….……. Interatomic force constant

K …….…..……..……. Kelvin

KS …….…….……. Kohn-Sham

LANL2DZ ……..…..…… Los Alamos National Laboratory 2-double-z

LDA …….……..……. Local density approximation

lp …….……... Lone-pair

LSDA …….……. Local spin density approximation

LUMO …….…….……. Lowest unoccupied molecular orbital

MD …….…….. Molecular dynamics

MP …….……..……. Monkhorst and Pack

NCPP …….……. Norm conserving pseudopotential

NHL ……..…….……..……. Nosé-Hoover-Langevin

NPT …….……..……. Isothermal-isobaric ensemble

NVT ……..……..… Constant volume –constant temperature ensemble

PAW …….…..……. Projector augmented-wave

PBC ……. Periodic boundary condition

PBE ……..…….……. Perdew, Burke and Enzerhof

PES …….……..……. Photoelectron spectroscopy

PSO …….…..……. Particle swarm-intelligence optimization

P-T …….……...……. Pressure-Temperature

PW …….……...……. Plane wave

PW91 …….…….……. Perdew and Wang

SAM …….……. Self-assembled monolayers

SCF …….……. Self-consistent field

TDDFT ……...…… Time-dependent density functional theory

TPa …….…….……. TeraPasca

USPP ……..……. Ultra soft pseudopotential

VASP ……..……..……. Vienna Ab-initio Simulation Package

*v*DOS …….……..……. Vibrational density of states

VPSR ……..… Full electronic Darwin and mass-velocity relativistic effects

XRD …….……. X-ray diffraction

ZPE …….……. Zero-point energy

CHAPTER 1

INTRODUCTION

The world around us can be found to be filled with various micro and macromolecules of natural/biological or synthetic origin. These molecules may be a structural network of metals, alloys or composites extended in one, two or three dimensions. The understanding of their properties, ranging from electronic to super-ionic states is very paramount because they form a fabric for industrial and technological advancement [1-2]. Research in the area of energetic materials (EMs) has been actively pursued, which culminate into numerous experimental, analytical and computational models capable of evaluating or predicting the performance of EMs in various thermodynamic conditions. EMs are very important because they are capable of storing relatively large amount of energy which are readily deliverable. Thus, they have their application in explosives, where very rapid rate of energy application and high pressures are essential [3]. Recently, scientists in the EMs community has been faced with the challenge of synthesizing energetic compounds with great chemical stability and highest possible density. This problems, in part, can be solved by computationally designing and characterizing a desired EM before laboratory synthesis. The advantage of such approach is the possibility of exploring large number of geometrical combination of base chemical elements that make up the EM at a relatively cheap cost than actual laboratory combinatory experiments. The particle swarm-intelligence optimization (PSO) algorithm is a powerful computer algorithm that open the possibility of computationally designing materials without prior knowledge of their crystal structure. This unique capability along

side the social intelligence feature makes it effective for designing materials of varying dimensions ranging from the bulk 3D materials (such as EMs) up to 2D, 1D and 0D clusters.

The recent boom in the field of catalysis has open up research into the design of bimetallic clusters formed solely from the atoms of two different metallic elements. It is well accepted that catalysts made of two metals can be achieved by establishing a contact between two suitable carriers such as silica with an aqueous precursor solution of salts containing metals of interest [4]. For a very long time, synthesis, characterization and study of bimetallic clusters has been limited to experimental and chemical approaches alone. Computational exploration is necessary for this task as the need to cut down on the size of materials applicable in nanoelectronics become very pressing. To this end, the need to rationalize the growth mechanism from the cluster to crystalline phase in this new family of material is anticipated to lead to new discovery in nanomaterials research.

This work is thus designed to computationally explore and solve structural evolution problems between the two extremes of material class – the 3 D bulk material class up to the 0 D clusters. Nitrogen, a high energy density material (HEDM) which have found application in explosives' design alongside bimetallic nanoclusters which have found application in catalysis will be studied in details. The study will cut across prediction of their crystal structures using the PSO and careful characterization using first principles approach with the aim of contributing to the understanding of layered polymeric phase of Nitrogen at extreme thermodynamic conditions and cluster growth at ambient conditions.

1.1 Density functional theory

The description of the structures and dynamics of many-electron system is one of the early but basic problems in theoretical physics and chemistry. The many-particle nature of realistic systems called for some more robust formalisms beyond the reach of the classical physical laws. Density functional theory (DFT) [5-7] was introduced in 1963 by Kohn *et al.* [8], as an effective approach to obtain approximate solutions to the many-particle problems. DFT is conceptually rooted in the Thomas-Fermi model of a uniform electron gas [9], coupled with the Slater local exchange approximation [10]. Within the DFT framework, the ground state of a crystal structure is mapped to the ground-state electron density in a way that the Schrödinger wave equation,

$$\widehat{H}\psi(\boldsymbol{r}_1, \dots, \boldsymbol{r}_n) = E\psi(\boldsymbol{r}_1, \dots, \boldsymbol{r}_n), \tag{1.1}$$

is satisfied for many-particle system. *Ab initio* (first principles) theory in which DFT is a part, embraces all essentially non-empirical and wavefunction-based methods of solving the Eq. (1.1) for many-particle systems [11]. The Schrödinger wave equation for many-particle system is called the Kohn-Sham (KS) equation [8]. Particles in many-particle systems continually interact, which make constructing analytical solutions to the KS equation close to impossible. Thus, development of approximate-solution schemes has evolved with each scheme having its own assumptions. For example, the Born-Oppenheimer approximation was built on the premise that the nucleus of an atom is about 1800 times more massive than the electron, justifying the treatment of the nucleus as stationary relative to the electron. Thus, the many-particle system is mapped into a system of non-interacting single particles (pseudo particles) [11]. The ground-state electron density which is the only physical observable of the DFT is then built from the solutions to the KS equations (KS orbitals) of each electron. Interesting properties ranging from electronic structure, lattice vibration, superconductivity, magnetic properties, to bonds and bond characterization were successfully

studied using this theory [7]. A variation of DFT that is effective in studying properties of system in the excited state is the time-dependent density functional theory (TDDFT).

1.1.1 Kohn-Sham formulation of DFT

Many-particle system obeying the Hamiltonian for the system of electrons and nuclei,

$$\hat{H} = -\frac{\hbar^2}{2m_e}\sum_i \nabla_i^2 - \sum_{i,I}\frac{Z_I e^2}{|\boldsymbol{r}_i - \boldsymbol{R}_I|} + \frac{1}{8\pi\varepsilon}\sum_{i\neq j}\frac{e^2}{|\boldsymbol{r}_i - \boldsymbol{r}_j|} - \sum_I \frac{\hbar^2}{2M_I}\nabla_I^2 + \frac{1}{8\pi\varepsilon}\sum_{I\neq J}\frac{Z_I Z_J e^2}{|\boldsymbol{R}_I - \boldsymbol{R}_J|}\ , \tag{1.2}$$

where electrons are denoted by lower case subscripts and nuclei, with charge Z_I and mass M_I, denoted by upper case subscripts was replaced with a different auxiliary system that can be solved more easily, ε is the permittivity of the system. In a more compact form, Eq. (1.2) can be written as

$$\hat{H} = \hat{T} + \hat{V}_{ext} + \hat{V}_{ee} + \hat{V}_{NN} \tag{1.3}$$

where

$$\hat{T} = -\frac{1}{2}\sum_{i=1}^{N}\boldsymbol{\nabla}_i^2\ , \hat{V}_{ee} = \frac{1}{2}\sum_{i\neq j}\frac{1}{|\boldsymbol{r}_i - \boldsymbol{r}_j|}\ , \hat{V}_{NN} = -\sum_I \frac{1}{2M_I}\nabla_I^2\ , \hat{V}_{ext} = \sum_{i,I}\frac{Z_I}{|\boldsymbol{r}_i - \boldsymbol{R}_I|} + \frac{1}{2}\sum_{I\neq J}\frac{Z_I Z_J}{|\boldsymbol{R}_I - \boldsymbol{R}_J|}\,. \tag{1.4}$$

In this equation (Eq. 1.4) as well as throughout this review, the atomic units are used with $\hbar = 1$, $m_e = 1$ and $e = 1$. Furthermore, $\boldsymbol{r}_i$ is the position of the *i-th* electron, $V_{ext}(\boldsymbol{r})$ is a measure of

Coulomb interaction, in term of potential between the electrons and the nuclei. N is the number of electrons in the system, $\hat{V}_{ee}$ is the electron-electron repulsion term, $\hat{V}_{NN}$ is the nuclear-nuclear repulsion term and $\hat{T}$ is the kinetic energy operator. The most common implementation of DFT have been done through the KS equations which conceptually rely on the continual validity of the statement of existence by Hohenberg-Kohn, colloquially referred to as the Hohenberg-Kohn (HK) theorem [7]. The first HK theorem is only an existence theorem which is based on the premise that there exists a one-to-one mapping between the ground state electron density (see Eq. 1.7) and the ground state wavefunction but skipped the mathematical description of such mappings. It is in these mappings that approximations are made. The two HK theorems can be stated as:

Theorem 1.1.1 ([6-7])**.** *The ground-state energy from Schrödinger's equation is a unique functional of the electron density.*

Proof. Consider the electron density ρ for the ground state electron density of some N-electron system. If we assume that there are two external potentials V_{ext} and V'_{ext}, different by more than a constant and suppose the two external potentials give the same ρ for its ground state, then there exists two Hamiltonians $\hat{H}$ and $\widehat{H'}$ corresponding to the same ground state density but different normalized N-electron wavefunctions ψ and ψ'. If we designate ψ' as a trial function for the Hamiltonian $\hat{H}$, we can construct a proof by contradiction as follows

$$E_0 < \langle \psi' | \hat{H} | \psi' \rangle = \langle \psi' | \widehat{H'} | \psi' \rangle + \langle \psi' | \hat{H} - \widehat{H'} | \psi' \rangle$$

$$= E'_0 + \int \rho(\boldsymbol{r}) \, [V_{ext}(\boldsymbol{r}) - V'_{ext}(\boldsymbol{r})] d\boldsymbol{r} \, , \qquad (1.5)$$

where E_0 and E'_0 are the ground-state energies corresponding to $\hat{H}$ and $\widehat{H'}$, respectively. Repeating the procedure above with a trial function ψ for the Hamiltonian $\widehat{H'}$, yields:

$$E_0' < \langle\psi|\widehat{H'}|\psi\rangle = \langle\psi|\widehat{H}|\psi\rangle + \langle\psi|\widehat{H'} - \widehat{H}|\psi\rangle$$

$$= E_0 + \int \rho(\boldsymbol{r})\,[V_{ext}(\boldsymbol{r}) - V'_{ext}(\boldsymbol{r})]d\boldsymbol{r}\,. \tag{1.6}$$

Adding Eqs. (1.5) and (1.6), we get the contradiction $E_0 + E_0' < E_0 + E_0'$, thus there cannot be two different V_{ext} corresponding to the same ρ for their ground states. It then follows that the ground-state energy from Schrödinger's equation is a unique functional of the electron density.

□

Theorem 1.1.2 ([6-7])**.** *The electron density that minimizes the energy of the overall functional is the true electron density corresponding to the full solution of the Schrödinger equation.*

Following an educated guess (which was later verified by results) Kohn and Sham [8] assumes that the ground state density of the original interacting system is equal to that of some chosen non-interacting (auxiliary) system. This simplifies the interacting-system problem to independent-particle equations for non-interacting system with all the cumbersome many-body terms incorporated into an exchange correlation functional of the density. Essentially, DFT can be viewed as a developed method in which the knowledge of one-electron density,

$$\rho(\boldsymbol{r}) = N \int d^3\boldsymbol{r}_2 \int d^3\boldsymbol{r}_3 \ldots \int d^3\boldsymbol{r}_N\, \psi^*(\boldsymbol{r}, \boldsymbol{r}_2, \ldots, \boldsymbol{r}_N)\psi(\boldsymbol{r}, \boldsymbol{r}_2, \ldots, \boldsymbol{r}_N), \tag{1.7}$$

implies knowledge of the wavefunction, the potential and by extension, all other observables. In principle, many-particle wavefunction depends on 3N variables, and each of the N particles depends on three spatial variables. However, in practice, DFT is only a function of the density which has three variables, thereby reducing the complexity that arise for system with large value of N.

From the first HK theorem, the Hamiltonian in Eq. (1.3) and the electron density in Eq. (1.7),

$$E[\rho] = T[\rho] + V_{ee}[\rho] + V_{NN}[\rho] + V_{ext}[\rho]. \tag{1.8}$$

The contribution of the external potential can be written explicitly in terms of the density as

$$V_{ext}[\rho] = \int V_{ext}(\boldsymbol{r})\, \rho(\boldsymbol{r}) d^3\boldsymbol{r}\ . \tag{1.9}$$

The functionals $T[\rho]$, $V_{ee}[\rho]$ and $V_{NN}[\rho]$ are known for a given system configuration and are called universal functionals. However, the functional $V_{ext}[\rho]$, which is system dependent is unknown. Given a system for which $V_{ext}(\boldsymbol{r})$ is known, substituting Eq. (1.9) into (1.8) and invoking the second HK theorem, it suffices to write

$$E[\rho] = T[\rho] + V_{ee}[\rho] + V_{NN}[\rho] + \int V_{ext}(\boldsymbol{r})\, \rho(\boldsymbol{r}) d^3\boldsymbol{r}\ , \tag{1.10}$$

and the ground-state energy of the system is derived by minimizing Eq. (1.10) with respect to $\rho(\boldsymbol{r})$.

If we attempt to write the functional described by the HK theorem in terms of single-particle wavefunctions, $\psi_i(\boldsymbol{r})$, and bearing in mind that Eq. (1.7) defines the electron density, then, the energy functional can be written as

$$E[\{\psi_i\}] = E_{analytic}[\{\psi_i\}] + E_{XC}[\{\psi_i\}], \tag{1.11}$$

where $E_{analytic}$ is a collection of terms whose analytical form is completely known and every other terms including all the quantum mechanical effects not described by the analytical form are represented as E_{XC}. The analytic term in terms of contribution can be explicitly defined as

$$E_{analytic}[\{\psi_i\}]$$

$$= -\frac{1}{2}\sum_i \int \psi_i^* \boldsymbol{\nabla}^2 \psi_i d^3r + \int V(\boldsymbol{r})\rho(\boldsymbol{r}) d^3r + \frac{1}{2}\iint \frac{\rho(\boldsymbol{r})\rho(\boldsymbol{r}')}{|\boldsymbol{r}-\boldsymbol{r}'|} d^3r d^3r'$$

$$+ E_{ion}\,. \qquad (1.12)$$

E_{ion} in Eq. (1.12) is the Coulomb interactions between pair of nuclei, the first, second and third terms are the electron kinetic energies, Coulomb interactions between the electrons and the nuclei and the Coulomb interactions between pair of electrons, respectively. Kohn and Sham went further to show that finding the right electron density can be done by solving a set of equations in which each equation only involves single electron. Thus, they put forward the KS equation that has the form

$$\left[-\frac{1}{2}\boldsymbol{\nabla}^2 + V(\boldsymbol{r}) + V_H(\boldsymbol{r}) + V_{XC}(\boldsymbol{r})\right]\psi_i(\boldsymbol{r}) = \varepsilon_i \psi_i(\boldsymbol{r})\,. \qquad (1.13)$$

The solutions to equation (1.13) are single-particle wavefunctions that are dependent on three spatial variables only. $V(\boldsymbol{r})$ defines the interactions between an electron and the collection of atomic nuclei. The Hartree potential, $V_H(\boldsymbol{r})$, is the Coulomb repulsion between the effective electron density of all electrons and the *i-th* electron being considered in the KS equation. In a manner of speaking, the $V_H(\boldsymbol{r})$ already factor in the self-interaction contribution, since the *i-th* electron as well contribute to the effective electron density. Mathematically,

$$V_H(\boldsymbol{r}) = \int \frac{\rho(\boldsymbol{r}')}{|\boldsymbol{r}-\boldsymbol{r}'|} d^3r'. \qquad (1.14)$$

The exchange-correlation term, $V_{XC}(\boldsymbol{r})$, yield an exchange-correlation energy functional $E_{XC}[\rho(\boldsymbol{r})]$ which can be separated into the exchange part $E_X[\rho(\boldsymbol{r})]$ as well as the correlation part $E_C[\rho(\boldsymbol{r})]$. The analytical definition of $V_{XC}(\boldsymbol{r})$ is thus

$$V_{XC}(\boldsymbol{r}) = \frac{\delta E_{XC}[\rho(\boldsymbol{r})]}{\delta \rho(\boldsymbol{r})} . \tag{1.15}$$

Putting Eqs. (1.14) and (1.15) into Eq. (1.13) yields

$$\left[-\frac{1}{2}\boldsymbol{\nabla}^2 + V(\boldsymbol{r}) + \int \frac{\rho(\boldsymbol{r}')}{|\boldsymbol{r}-\boldsymbol{r}'|} d^3r' + \frac{\delta E_{XC}[\rho(\boldsymbol{r})]}{\delta \rho(\boldsymbol{r})}\right]\psi_i(\boldsymbol{r}) = \varepsilon_i \psi_i(\boldsymbol{r}) . \tag{1.16}$$

So far, we have established that the problem of a system of interacting particles can be formulated into and approximated by an auxiliary system of non-interacting particles, if their ground state energy can be mapped (HK theorems). Also, that the accuracy of predictions done using this auxiliary system depends on how well the map performs and that the KS equations gives the mechanics of the auxiliary system. Solving the KS equations requires the knowledge of the Hartree potential, which requires the knowledge of electron density. The knowledge of the electron density requires the knowledge of the single-particle wavefunctions, which requires solving the KS equation. Hence, constructing solutions for this type of problem requires an iterative method.

1.1.2 Functionals for exchange and correlation

The KS DFT is continually being employed in the study of electronic and other properties of materials and solids because of the success of approximate functionals that were able to reproduce experimental observations to a significant degree of accuracy. In practice, the KS formalism, though beautiful and compact, yet is unsolvable because of the exchange-correlation

($E_{XC}(\rho)$) term present in Eq. (1.16). To make the construction of solutions to this equation less cumbersome and achievable, approximations were made for the $E_{XC}(\rho)$ term whose exact form is unknown. So far, great progress has been made with the following remarkably simple approximations:

1.1.2.1 The local spin density approximation (LSDA)

If we assume as Kohn and Sham [8] did, that solids are close to the limit of homogeneous electron gas, then we can make an approximation about the local spin density being constant over all space as in a homogeneous electron gas. Thus, exchange-correlation energy functional takes the form

$$E_{XC}^{LSDA}\left[\rho^{\uparrow},\rho^{\downarrow}\right]=\int d^{3}r\,\rho(\boldsymbol{r})\epsilon_{XC}^{uniform}\left(\rho^{\uparrow}(\boldsymbol{r}),\rho^{\downarrow}(\boldsymbol{r})\right). \tag{1.17}$$

The exchange-correlation term can be written as a direct sum of the exchange energy per electron, which is known exactly in its analytic form, and the correlation term

$$E_{XC}^{LSDA}\left[\rho^{\uparrow},\rho^{\downarrow}\right]=\int d^{3}r\,\rho(\boldsymbol{r})\left[\epsilon_{X}^{uniform}\left(\rho^{\uparrow}(\boldsymbol{r}),\rho^{\downarrow}(\boldsymbol{r})\right)+\epsilon_{C}^{uniform}\left(\rho^{\uparrow}(\boldsymbol{r}),\rho^{\downarrow}(\boldsymbol{r})\right)\right]. \tag{1.18}$$

The problem of double-counting of interaction is taken into account in the construction of the exchange contribution to average energy per electron by multiplying the contribution to energy eigenvalue by a factor of $\frac{1}{2}$. Thus yielding

$$\epsilon_{X}=-\frac{1}{2}\frac{3}{2\pi}k_{F}^{\sigma}=-\frac{3}{4}\left(\frac{6}{\pi}\rho^{\sigma}\right)^{1/3}, \tag{1.19}$$

where k_F^σ is the spin-polarized Fermi wave number as a function of spin-polarized electron density ρ^σ. The correlation energy to a great accuracy have been calculated using Monte Carlo methods for homogeneous electron gas with different kind of electron densities [12-13]. The LSDA is expected to be best for such systems that mimic the behaviour of a homogeneous gas, such as a nearly-free-electron metal. However, this approximation performs poorly for such systems of atoms where the density must go continuously to zero outside the atom. This down side of LSDA has stimulated ideas for constructing functionals that are expected to perform better for such systems for which the LSDA failed.

1.1.2.2 The generalized-gradient approximations (GGA)

Another form of approximation to the KS functional expected to achieve better (though not in all cases) results than the LSDA is the generalized-gradient approximation. The premise upon which the approximation is based is the fact that real materials do not have a uniform electron density, rather a slowly varying one. Thus, GGA functional is expressed using both the local electron density and the spatial variation in the electron density captured through the density gradient. The generalized form of the GGA functional is

$$E_{XC}^{GGA}[\rho^\uparrow, \rho^\downarrow] = \int d^3r\, \rho(\boldsymbol{r}) \epsilon_{XC}(\rho^\uparrow, \rho^\downarrow, |\boldsymbol{\nabla}\rho^\uparrow|, |\boldsymbol{\nabla}\rho^\downarrow|, \dots)$$

$$\equiv \int d^3r\, \rho(\boldsymbol{r}) \epsilon_X^{uniform}(\rho) F_{XC}(\rho^\uparrow, \rho^\downarrow, |\boldsymbol{\nabla}\rho^\uparrow|, |\boldsymbol{\nabla}\rho^\downarrow|, \dots), \qquad (1.20)$$

Where $\epsilon_X^{uniform}(\rho)$ is the exchange energy of the unpolarised gas and F_{XC} is the exchange enhancement factor. The F_{XC} can be written in term of the of the dimensionless reduced density gradients of m_{th} order and can be defined by

$$S_m(\boldsymbol{r}) = \frac{|\boldsymbol{\nabla}^m \rho(\boldsymbol{r})|}{(2k_F)^m \rho(\boldsymbol{r})} = \frac{|\boldsymbol{\nabla}^m \rho(\boldsymbol{r})|}{2^m (3\pi^2)^{m/3} (\rho(\boldsymbol{r}))^{(1+m/3)}} \,. \tag{1.21}$$

The value of F_{XC} varies with different types of approximation in use. Available approximations include but not limited to the Becke (B88) [14-15], Perdew and Wang (PW91) [16], and Perdew, Burke and Enzerhof (PBE) [17]. However, the most widely used approximation is the PBE. The improvements of PBE over PW91 include an accurate description of the linear response of the uniform electron gas, correct behaviour under uniform scaling and a smoother potential. The formalism of PBE was started with the GGA for correlation in the form

$$E_C^{PBE}\left[\rho^{\uparrow}, \rho^{\downarrow}\right] = E_C^{GGA}\left[\rho^{\uparrow}, \rho^{\downarrow}\right] = \int d^3r \; \rho[\epsilon_C^{uniform}(r_s\,, \zeta) + H(r_s, \zeta, t)] \,, \tag{1.22}$$

Where r_s is the local Seitz radius, $\rho = 3/(4\pi r_s^3) = k_F^3/3\pi^2$, $\zeta = (\rho^{\uparrow} - \rho^{\downarrow})/\rho$ is the relative spin polarization, and $t(\boldsymbol{r}) = |\boldsymbol{\nabla}\rho(\boldsymbol{r})|/2\phi\, k_s \rho(\boldsymbol{r})$ is a dimensionless density gradient [14-15, 17-19]. $\phi(\zeta) = \left[(1+\zeta)^{2/3} + (1-\zeta)^{2/3}\right]/2$ is a spin scaling factor and $k_s = 2\sqrt{k_F/\pi}$ is the Thomas-Fermi screening wave number. The gradient contribution $H(t, r_s, \zeta)$ was constructed from three conditions:

(a) In the slowly varying limit ($t \to 0$), $H(t, r_s, \zeta)$ is given by its second-order gradient expansion [13-15]

$$H(t, r_s, \zeta) \to \beta \phi^3 t^2 \,, \tag{1.23}$$

where $\beta \cong 0.066725$.

(b) In the rapidly varying limit $t \to \infty$, $H(t, r_s, \zeta) \to -\epsilon_C^{uniform}$, this makes correlation to vanish.

(c) Under uniform scaling to the high density limit, the correlation energy must scale to a constant [13]. Thus, $H(t, r_s, \zeta) \to \gamma \phi^3 \ln t^2$, where $\gamma = (1 - \ln 2)/\pi^2 \cong 0.031091$.

Hence, conditions (a) – (c) are satisfied by

$$H(t, r_s, \zeta) = \gamma\phi^3 \ln\left\{1 + \frac{\beta}{\gamma} t^2 \left[\frac{1+At^2}{1+At^2+A^2t^4}\right]\right\}, \tag{1.24}$$

where

$$A = \frac{\beta}{\gamma}\left[\exp\left\{\frac{-\epsilon_C^{uniform}}{\gamma\phi^3}\right\} - 1\right]^{-1}. \tag{1.25}$$

The GGA for the exchange energy was also constructed [17] and the expression, for $\zeta = 0$ everywhere, was derived to be

$$E_X^{PBE} = E_X^{GGA} = \int d^3r\, \rho\epsilon_X^{uniform}(\rho) F_X^{PBE}(s), \tag{1.26}$$

where $\epsilon_X^{uniform} = -3k_F/4\pi$ and $F_X^{PBE}(s) = 1 + \kappa - \frac{\kappa}{(1+\mu s^2/\kappa)}$, with $\kappa = 0.804$, $\mu = 0.235$.

The PBE (GGA) approximation of the exchange-correlation energy functional have recorded much success in the study of structural geometry, atomic total energy and vibrational properties of systems whose electron density varies slowly in space [20]. This success can be attributed, in part, to the inclusion of more physical ingredient than the LSDA. The efficacy of PBE functional in structural parameters prediction is demonstrated in the study of systems of C, O, Si [21], where such predictions were shown to agree very well with experimental observations.

1.1.3 The periodic boundary condition

Completion of the formalism of the KS DFT and various approximations to the exchange-correlation functional was a breakthrough. However, applying it to a real solid system or other condensed matter poses another dimension of challenge due to the very large number of non-

interacting electrons (on the order of Avogadro's number) involved. It is quite interesting that crystalline solids are composed of spatially repeating units. Thus, solving the Schrödinger equation in a unit cell suffices for the whole crystalline solid by taking advantage of the periodicity of the crystal. This leads to the use of periodic boundary condition (PBC) via the Bloch theorem. The Bloch theorem states that the wavefunctions of the crystal Hamiltonian can be written as

$$\psi_i(\boldsymbol{k},\boldsymbol{r}) = e^{i\boldsymbol{k}\cdot\boldsymbol{r}}u_i(\boldsymbol{k},\boldsymbol{r}), \tag{1.27}$$

where $u_i(\boldsymbol{k},\boldsymbol{r})$ denote the periodic functions also known as the Bloch wavefunctions for which $u_i(\boldsymbol{k},\boldsymbol{r}) = u_i(\boldsymbol{k},\boldsymbol{r}+\boldsymbol{R})$ for all lattice vector $\boldsymbol{R}$. The Bloch wavefunctions extend on the whole crystals and thus have a delocalized nature [22]. This theorem is a direct consequence of translational symmetry of the crystal which satisfies

$$\psi_i(\boldsymbol{k},\boldsymbol{r}+\boldsymbol{R}) = e^{i\boldsymbol{k}\cdot\boldsymbol{R}}\psi_i(\boldsymbol{k},\boldsymbol{r})\,. \tag{1.28}$$

1.1.4 *k*-point sampling

Substituting Eq. (1.28) into Eq. (1.16) does not necessarily make solving the resulting equation any simpler, rather, it opens up a problem of integrating periodic functions of Bloch wave vector over either the entire Brillouin zone (BZ) or over specified portions. Therefore, the system of eigen-equations grow infinitely because each eigen-equation is evaluated at each k-point with the BZ containing infinite number of k-points. To optimize the calculations, it is necessary to compute these functions only at a carefully selected set of points in the BZ. If we assume that electronic wavefunctions with close enough proximity to each other will be almost identical, then, an electronic wavefunction at a carefully chosen single k-point in the reciprocal space suffices to represent groups of electronic wavefunctions whose k-points satisfy the proximity criteria. This

task obviously begs for an efficiently optimized numerical integration and interpolation scheme. The most widely used scheme for the k-point sampling was developed by Monkhorst and Pack [23] in 1976. Monkhorst and Pack developed the so called MP mesh. The mathematical formalism of the MP mesh is set out to integrate a function $f(\boldsymbol{k})$ that is totally symmetric and periodic in $\boldsymbol{k}$-space. Thus, $f(\boldsymbol{k})$ can be expanded in $B_i(\boldsymbol{k})$,

$$f(\boldsymbol{k}) = \sum_{i=1}^{\infty} f_i B_i(\boldsymbol{k}) \,, \tag{1.29}$$

where, due to orthogonality of $B_i(\boldsymbol{k})$ on the BZ,

$$f_i = \frac{v}{8\pi^3} \int_{BZ} d\boldsymbol{k}\, B_i^*(\boldsymbol{k}) f(\boldsymbol{k}) \,. \tag{1.30}$$

Therefore, the integral of $f(\boldsymbol{k})$ over the entire BZ leads to

$$\int_{BZ} d\boldsymbol{k}\, f(\boldsymbol{k}) = \frac{v}{8\pi^3} f_1 \,. \tag{1.31}$$

An approximation to Eq. (1.30) can be obtained over the set of $\boldsymbol{k}_j$ points as

$$\check{f}_i = \frac{1}{q^3} \sum_{j=1}^{P(q)} w_j f(\boldsymbol{k}_j) B_i(\boldsymbol{k}_j) \,, \tag{1.32}$$

and

$$\check{f}(\boldsymbol{k}) = \sum_{\boldsymbol{i}} \check{f}_{\boldsymbol{i}} B_i(\boldsymbol{k}) \,, \tag{1.33}$$

where $P(q)$ is the symmetry-dependent number of points $\boldsymbol{k}_j$ in the irreducible wedge of the BZ and w_j is the weight associated with the point $\boldsymbol{k}_j$. The associated error for the approximation of equation (1.31) using Eq. (1.33) is

$$\epsilon_{BZ} = \int_{Bz} d^3r \left[f(\boldsymbol{k}) - \check{f}(\boldsymbol{k}) \right]. \tag{1.34}$$

For the case where the integration is over a portion of the BZ, enclosing a volume V, then the integral can be represented by

$$\int_V d\boldsymbol{k}\, f(\boldsymbol{k}) \approx \sum_i \check{f}_i \int_V d\boldsymbol{k}\, B_i. \tag{1.35}$$

When the k-points mesh used in sampling the BZ is dense enough, then the error in computed total energy, quantified by Eq. (1.34), approaches zero. When this number is small enough (within some confidence level) then we say that convergence has being achieved in the k-point sampling of the BZ.

1.1.5 The planewave basis set

In principle, an infinite number of plane wave (PW) basis set is required to fulfil the expansion proposed through the Bloch theorem. However, the second part of Eq. (1.28) can be expanded into a finite number of plane waves for which wave vectors correspond to the reciprocal lattice vectors of the crystal. Thus, each eigen-function of the KS (corresponding to each electronic wavefunction) equation is a sum of plane waves, with normalization constant ϖ :

$$\psi_i(\boldsymbol{k},\boldsymbol{r}) = \frac{1}{\sqrt{\varpi}}\sum_{\boldsymbol{G}} c_{i,\boldsymbol{k}+\boldsymbol{G}} \cdot e^{\boldsymbol{i}(\boldsymbol{k}+\boldsymbol{G})\cdot\boldsymbol{r}} \ . \tag{1.36}$$

In practice, the coefficient, $C_{\boldsymbol{i},\boldsymbol{k}+\boldsymbol{G}}$ (where $\boldsymbol{G}$ are reciprocal lattice vectors) which corresponds to small kinetic energies $|\boldsymbol{k}+\boldsymbol{G}|^2$ are more important in the Bloch expansion than those with large kinetic energies. Thus, the PW basis set can be truncated to include only plane waves that have kinetic energies that are smaller than some particular cutoff energy. In a more mathematical sense, this criterion requires that the kinetic energies of the basis set be less than the cutoff energy,

$$E_{cut} > \tfrac{1}{2}|\boldsymbol{k}+\boldsymbol{G}|^2 \ . \tag{1.37}$$

The idea of choosing cutoff energy often lead to an error in the computed total energy and its derivatives. However, in practice, cutoff energy should be increased until the calculated total energy converges within the required tolerance. This ensures that the error introduced through an incomplete basis set as a result of plane wave energy cutoff is reduced to within some tolerance [24-26].

1.1.6 The Pseudopotential approximation

In the region near a nucleus there is a strong bonding between the nucleus and the electron which give rise to a localized wavefunctions in the region near the nucleus. The task of expanding a localized (core) wavefunction is computationally expensive; at the same time, the need to include relativistic and other effects in DFT calculation is on the rise, making such task more expensive. This peculiar situation calls for an approximation that can improve DFT calculations, reduce the basis set size while conserving computer time and resources. It is well known that physical properties of most matter depends more on the bonding system between atoms that make up the

matter and in turn, the bonding depends on the valence (not the core) electrons. Hence, an approximation that consider only the wavefunctions of valence electrons outside the core during PW expansion is not unphysical. Furthermore, nearest neighbour atoms do not have their cores interact significantly and for this reason, the electronic structure is gently influenced. The advantage of these assumptions and approximation is that the very high energy cutoff E_{cut} required for the PW expansion in the localized region can be avoided without giving up the physical details of the system under study. The approximations were implemented [27-30] by replacing the core electrons and the ionic potentials by pseudopotential which acts on set of pseudo wavefunctions instead of the true valence wavefunctions. Orthogonality of the pseudo wavefunctions with the core wavefunctions is not necessarily required which leads to the possibility of representing the core wavefunction by a nodeless function. Consequently, very few PWs are required in the pseudo wavefunction's expansion.

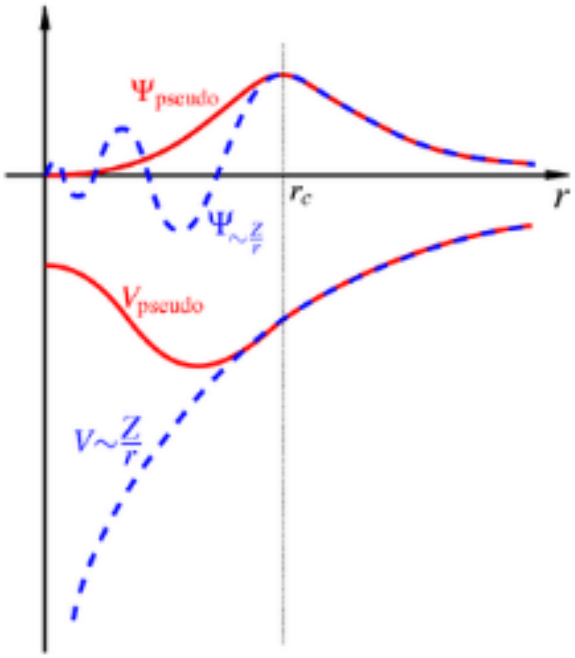

Figure 1.1. An all-electron valence wavefunction and electronic potential (dotted-blue curves) of the nucleus plotted against distance, r, from the atomic nucleus. Beyond the cutoff radius r_c, the

pseudo wavefunction and pseudo potential are identical to the all-electron valence wavefunction and potential, respectively. Ref. [31].

There are basically two forms of pseudopotentials, namely the norm conserving (NCPP) and the ultra soft (USPP). NCPP are constructed to fulfil two conditions which are

1. Inside the cutoff radius r_c, the norm of each pseudo wavefunction must be identical to the its corresponding all-electron wavefunction.

$$\int_{r<r_c} d^3r\, \psi_{R,i}(\boldsymbol{r})\, \psi_{R,j}(\boldsymbol{r}) = \int_{r<r_c} d^3r\, \psi_{pseudo_{R,i}}(\boldsymbol{r}) \psi_{pseudo_{R,j}}(\boldsymbol{r}) \qquad (1.38)$$

where $\psi_{R,i}$ and $\psi_{pseudo_{R,j}}$ are the all-electron and pseudo reference states, respectively, for the pseudopotential on atom R.

2. All-electron and pseudo wavefunctions are identical outside the cutoff radius, r_c.

The USPP is able to achieve a reduced basis set size by introducing a generalized eigenvalue problem with a non-zero difference in norms, so that a normalized eigenstate of the pseudo Hamiltonian obeys the generalized equation

$$\hat{H}\left|\psi_i(\boldsymbol{r})\right\rangle = \varepsilon_i \hat{S}\left|\psi_i(\boldsymbol{r})\right\rangle, \qquad (1.39)$$

where

$$\hat{S} = 1 + \sum_{R,i,j} |P_{R,i}\rangle q_{R,ij} \langle P_{R,j}| \;,\; q_{R,ij} = \left\langle \psi_{R,i}(\boldsymbol{r}) \middle| \psi_{R,j}(\boldsymbol{r}) \right\rangle - \left\langle \psi_{pseudo_{R,i}}(\boldsymbol{r}) \middle| \psi_{pseudo_{R,j}}(\boldsymbol{r}) \right\rangle$$

and $P_{R,i}$ are projectors that form a dual basis with the pseudo reference states within the cutoff radius and zero outside, such that

$$\left\langle P_{R,i} \middle| \psi_{pseudo}{}_{R,j}(\boldsymbol{r}) \right\rangle_{r<r_c} = \delta_{ij} \,. \tag{1.40}$$

Consequently, USPP are usually characterized by longer cutoff radius than the NCPP.

1.1.7 The PAW method

Blöchl, in 1994 [43] developed the Projector Augmented Waves (PAW) which is an all-electron scheme. The main idea carried by this method is that all-electron wave function can be constructed as a sum of the pseudo-wave function outside the core region and that of the partial wave function inside the core region less by the corresponding pseudo partial wavefunction in the core region. Thus, if we define the all-electron partial waves as $\sum_\sigma \psi_n^\sigma(\boldsymbol{r})$ and the pseudo waves as $\sum_\sigma \tilde{\psi}_n^\sigma(\boldsymbol{r})$, then the reconstructed KS wave function can be written as

$$\psi_n(\boldsymbol{r}) = \tilde{\psi}_n(\boldsymbol{r}) - \sum_\sigma \tilde{\psi}_n^\sigma(\boldsymbol{r}) + \sum_\sigma \psi_n^\sigma(\boldsymbol{r}) \tag{1.41}$$

In general, the PAW method is used in this thesis for various electronic structure calculations, unless otherwise stated in the methodology. A pictorial illustration of this construction process is shown in Fig. 1.2.

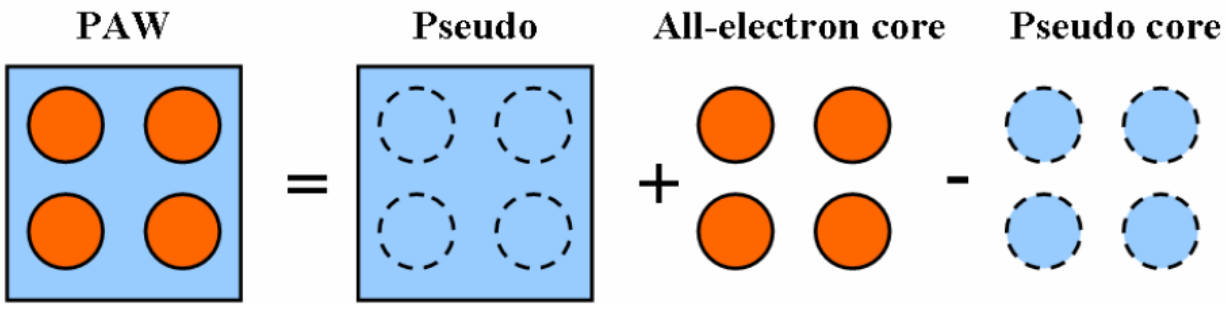

Figure 1.2. A simplified schematics of the procedures involved in the construction of PAW wave function with on-site and out-of-site contributions from all-electron and pseudo wavefunctions. Ref. [31].

1.1.8 Self-consistency and ground-state total energy

Finding the solutions to the KS equations for many-particle system requires the knowledge of other parameters (electron density, ground-state total energy) that depends on the solution (KS wavefunctions) itself. Thus, we can solve the KS equations iteratively using the self-consistent pseudopotential planewave method. The procedure used throughout this thesis for the calculation of electronic structure of various materials studied is described schematically in figure 1.3. The self-consistent field (SCF) calculation begins with an educated initial guess of the electron density $\rho(\boldsymbol{r})$. This guess is informed, in part, by the atomic density of chemical species that make up the system. The KS equations are then constructed using the guessed density and effective potential. The KS equation is solved numerically at each *k*-point throughout the BZ yielding a set of pseudo-wavefunctions. The pseudo-wavefunctions, which correspond to the KS orbitals, are used to calculate a new electron density $\rho_N(\boldsymbol{r}) = \sum_i |\psi_i(\boldsymbol{r})|^2$. The newly calculated electron density $\rho_N(\boldsymbol{r})$ is compared with the initially guessed density, $\rho(\boldsymbol{r})$, for convergence. Convergence is achieved if the difference $|\rho(\boldsymbol{r}) - \rho_N(\boldsymbol{r})|$ is less than some set tolerance, Ξ. If the tolerance criterion is not satisfied, the whole procedure is repeated again. This loop goes on and on with new density and reconstructed potential until convergence is achieved. Once convergence is achieved, the resulting electron density is used to calculate the ground-state total energy, which in turn is used to calculate the pseudo-wavefunction, energies (atomic energy levels / bands) as well as the force on each atom [32]. It is important to state that the pseudo-wavefunction contains information about other physical properties of the system being studied in the ground state. Hence, other physical properties of the system can be extracted from the pseudo-wavefunction.

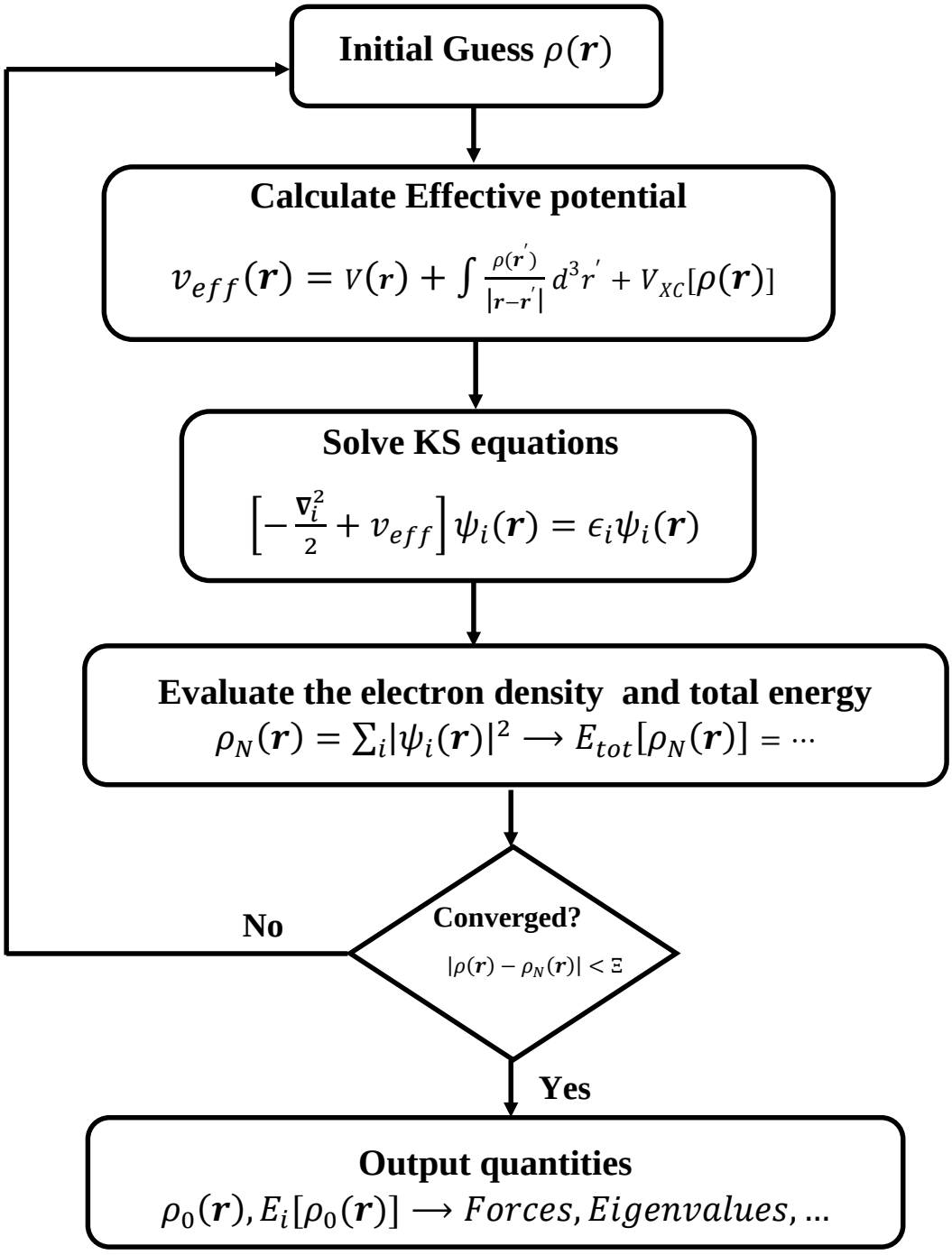

Figure 1.3. A flowchart illustrating how the self-consistent calculation proceeds step by step using DFT with PW basis set.

1.1.9 Particle swarm-intelligence optimization

A significant percentage of problems in condensed matter physics can be treated as an optimization problem. For example, when experimentalists measure various observables for their investigated system, theoretical understanding of the system always require solving its crystal structure. This particularly involves scanning the potential energy landscape of the chemical system, and finding a geometrical configuration of the system that minimizes its potential energy. Depending on the landscape of the potential, two types of optimal could exist: global or local. In most cases, the global as well as the local minimum potential energy is always degenerate over the surface. The particle swarm-intelligence optimization (PSO) algorithm is a stochastic, simulating and a modified form of random search algorithm. As a matter of fact, PSO and random search algorithm are both evolutionary in nature. In general, the PSO method, in addition to the contribution of the present motion, observe the close similarity between a swarm of particles, communicating with each other through individual and social knowledge, making it particularly suited for global exploration of the energy landscape. Furthermore, the collection of particles is assumed to be interacting through a classic Newtonian field [33]. PSO was developed under the assumption that optimization problems can be modelled as point flying as in a bird. The flight is made over mostly non linear and multidimensional space. The particle, through this algorithm is able to adjust its position in search space according to its own previous experience and that of its neighbouring particles. Generally, the point being considered is massless but considered a particle because of the presence of velocity vector. The velocity parameter is tuned in the clockwise (positive) or anticlockwise (negative) direction depending on how far away (and in what direction) from the best position the current value is. This powerful feature (which is lacking in random

search) makes PSO algorithm very intelligent and improve the convergence rate significantly. The general flow of process in the PSO method is shown in figure 1.4.

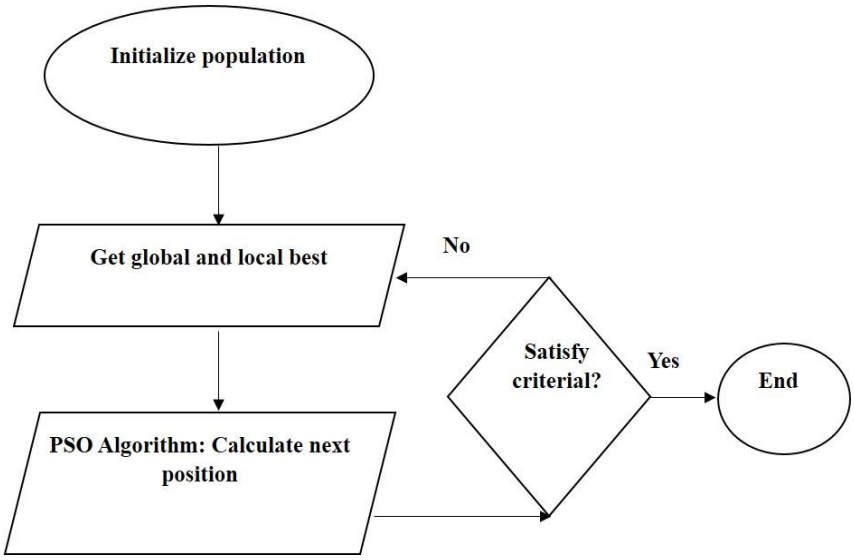

Figure 1.4. A flowchart illustrating how the particle swarm-intelligence optimization proceeds step by step [33].

1.2 Description of Physics at high pressure using DFT

Many laws of physics hold at extreme thermodynamic conditions, while some others are not effectively binding. This phenomenon is due to structural instability caused by increase in density, experienced by most ambient-stable structures at high temperature and pressure. Many DFT calculations are done at zero temperature and finite pressure. Thus, DFT (and its extended form, DFPT [32]) can be used in extensive exploration of properties of solids at high pressure. Few of the ways DFT and DFPT are employed for investigative study of solids at high pressure include the comparative stability measurement of different structures of the same material using

equations of state. Furthermore, the mechanical and dynamical stabilities of a phase can be investigated using phonon dispersion.

1.2.1. High-pressure equations of state

The equations of state (EOS) also known colloquially as phase diagram provides a framework to effectively compare the energies of structures with pressure. The Gibbs free energy provides a mathematical formulation that efficiently capture the effect of pressure-volume change, entropy and temperature change on the total energy of a system. Thus, mathematically, the Gibbs free energy $G = E - TS + pV$. Since we perform DFT calculations in this study at zero temperature, then entropy-temperature contribution vanishes. Therefore, the Gibbs energy of the system can be evaluated using the enthalpy ($G = E + pV = H$) without any loss of thermodynamic information. The EOS is derived by subjecting a crystal system (taken as a candidate structure) to an external pressure, which generates internal stress to the system. The compression (or decompression) is followed by minimization of the total energy through slightly constrained optimization of the crystal lattice, cell shape and atomic coordinates. At a finite pressure, the total energy corresponds to the enthalpy of the system at that pressure. An example EOS for candidate structures of BaCl at high pressure is shown in Fig. 1.5. We give the following interpretation to Fig. 1.5. The figure shows that the solid mixture Ba + $BaCl_2$ is stable up to 9 GPa, beyond which it adopts the *R-3m* structure between 9 GPa and 16 GPa. It then transforms to the B2 structure [34].

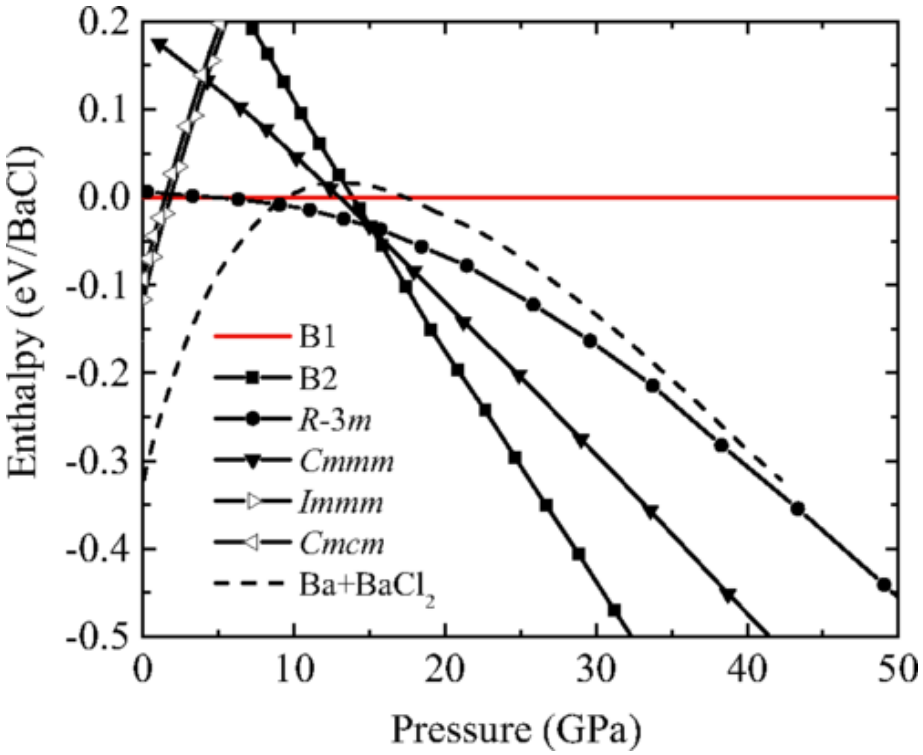

Figure 1.5. Equations of state phase diagram of barium chloride, with the B1 structure as the zero reference point [34].

In principle, calculation of structural changes depicted by EOS phase diagram generally require the knowledge of the forces

$$\boldsymbol{F}_I = -\frac{\partial E(\boldsymbol{R})}{\partial \boldsymbol{R}_I}\,, \tag{1.42}$$

and the stress tensor acting on each atom that makes up the chemical system. The equilibrium geometry of the system requires that equation (1.42) vanish. For this purpose, the Hellmann-Feynman theorem [35-36] is very useful. The Hellmann-Feynman theorem states that the first derivative of the eigenvalues of a Hamiltonian, H_λ, that depends on a parameter λ is given by the expectation value of the derivative of the Hamiltonian:

$$\frac{\partial E_\lambda}{\partial \lambda} = \left\langle \psi_\lambda \middle| \frac{\partial H_\lambda}{\partial \lambda} \middle| \psi_\lambda \right\rangle , \tag{1.43}$$

where ψ_λ is the eigenfunction of H_λ corresponding to the E_λ eigenvalue. Thus, from the Born-Oppenheimer approximation, we say that nuclear coordinates are the parameters of the electronic Hamiltonian, H_{BO}. We can therefore derive the force acting on the I_{th} nucleus in the electronic ground state as:

$$\boldsymbol{F}_I = -\frac{\partial E(\boldsymbol{R})}{\partial \boldsymbol{R}_I} = -\left\langle \psi(\boldsymbol{R}) \middle| \frac{\partial H_{BO}(\boldsymbol{R})}{\partial \boldsymbol{R}_I} \middle| \psi(\boldsymbol{R}) \right\rangle , \tag{1.43}$$

where $\psi(\boldsymbol{R})$ is the electronic ground state wave function of the Born-Oppenheimer Hamiltonian. In practice, we iteratively evaluate the ground-state energy, using DFT formalism and subject it to the Hellmann-Feynman theorem, evaluate the Hellmann-Feynman forces and examine if the difference between the calculated force in the previous and the present iteration is close to zero within a set tolerance (convergence criteria for the forces on atoms).

1.2.2. Structural stability

For the argument of stability of a material at high pressure to be thorough, it must simultaneously satisfy the condition of being energetically favourable and being mechanically and dynamically stable. Mechanical and dynamical stability are thus a measure of structural stability of the system. There are many established ways of investigating structural stability of a system which include, convex hull diagram [37-38] and phonon band structure [39]. In principle, a structure is said to be mechanically and dynamically stable at a given *P*-*T* condition if all frequencies at all *k*-points are greater than zero. In practice, frequencies are calculated at various high symmetry *k*-points chosen based on symmetry of the crystal structure being studied. Phonon dispersion band structure is then calculated by interpolating frequencies between two high

symmetry *k*-points through out the BZ. The presence of imaginary frequencies (usually represented as negative frequencies on the phonon band structure plot) can be interpreted as instability of a crystal structure at that *P*-*T* condition.

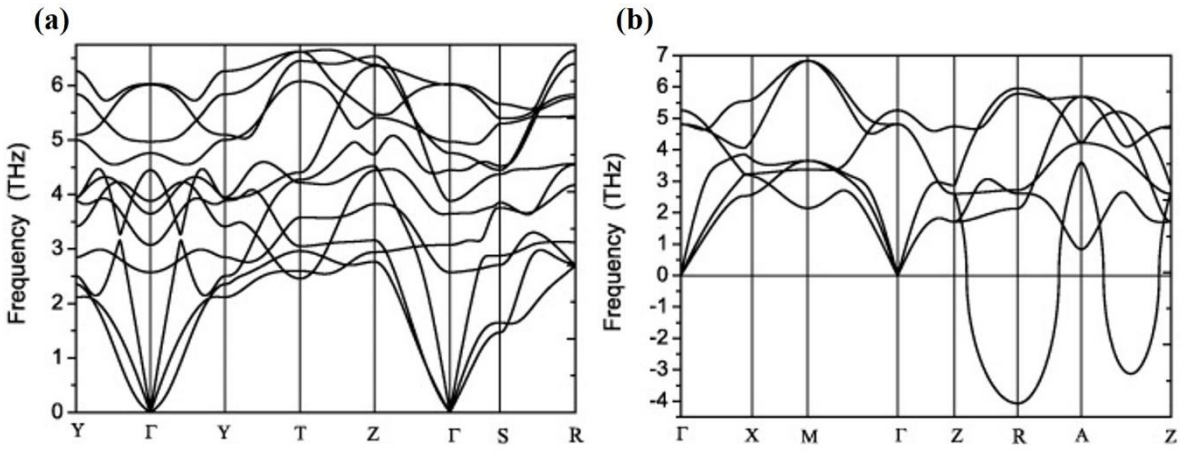

Figure 1.6. Phonon dispersions for(a) TaRu in the β'' structure (b) TaRu in the β'structure at ambient condition [40].

In the Fig. 1.6 above, vertical axes correspond to the phonon frequencies. It is observed in Fig. 1.6(a) that β'' structure of TaRu is mechanically and dynamically stable owing to the absence of negative frequencies. However, Fig 1.6(b) is characterized with negative frequencies, between *k*-points A and Z which implies that the β'structure of TaRu is mechanically and dynamically unstable. The horizontal axes represent the momentum axes marked at various high symmetry points in the BZ.

1.3 Description of this thesis

The objective of this thesis is to investigate novel solid materials that can be used in applications ranging from high energy density materials to semiconductor materials that can find

application in spintronic, thermoelectric, optoelectric and optoelectronic devices. Thus, our discussion will cover aspects of materials ranging from the theoretical crystal structure prediction to their characterization. The characterization will cover aspects such as the phase transition, lattice dynamics and electronic structure of these materials. First principles calculations involving DFT and DFPT were implemented using the VASP [41] code, interpolation of phonon frequencies throughout BZ were performed using the PHONOPY [42] code. Structural predictions are implemented through metadynamics and particle swarm-intelligence optimization method as implemented in the CALYPSO code.

1.3.1 VASP

VASP stands for *Vienna Ab-initio Simulation Package*. It is a first principles simulation package suitable for electronic structure calculation. The KS ground state is calculated in VASP using an iterative matrix diagonalization scheme and a self-consistency cycle with a Pulay mixer. Iterations run over electronic step and ionic step, thereby enabling two tiers of optimization – electronic optimization and ionic optimization. VASP employ planewave basis set in the determination of various properties of the system under study. Furthermore, the Blöchl's projector augmented-wave (PAW) electronic method is implemented within VASP [41]. The PAW method, which is another frozen-core electronic method, was originally introduced by Blöchl and was later adapted for plane wave calculations by Kressee and Joubert [43]. This method unlike the ultra soft pseudopotential method does not require specifying empirical parameters for each atom before being used.

1.3.2 PHONOPY

PHONOPY [42] is a phonon dispersion calculation program developed by Atsushi Togo. The PHONOPY code is interfaced with VASP for most of the calculations done with it, since it requires forces on atoms in a crystal which is evaluated using VASP. PHONOPY calculates phonon frequencies at various high-symmetry *k*-points within the BZ by constructing the interatomic force constant (IFC) matrix from forces on atoms using displacement method or force constant (FC) matrix using DFPT. The IFC or FC are then used to construct the dynamical matrix whose eigenvalues correspond to the phonon frequencies at a wave vector $\boldsymbol{k}$. The construction and symmetrization of FCs are implemented using singular-value decomposition. All phonon-related calculations implemented in PHONOPY are calculated using a supercell. Interfacing PHONOPY with VASP allows for the calculation of the gamma-point phonon frequencies for the supercell using finite difference method when displacement method is implemented in PHONOPY or the DFPT method when DFPT is implemented in PHONOPY. The dispersion is then calculated by interpolating the gamma-point frequencies through the various high-symmetry *k*-points.

1.3.3 CALYPSO

CALYPSO [44] is a global (exploration) optimization code which is interfaced with various local optimization codes such as VASP [41], SIESTA [45], QUANTUM ESSPRESSO [46] and ABINIT [47] to achieve best possible performance. The CALYPSO simulation scans the potential energy surface of a given chemical species for the global minimum potential energy using the particle swarm-intelligence algorithm (PSO). The CALYPSO code through the PSO algorithm makes few or no assumptions about the solutions of the given potential function. Furthermore, it can search very large space for candidate solutions by moving them in the search space over the

particles' positions and velocities with fast convergence. In addition to symmetry constraints (which significantly reduce the search space by utilizing structure diversity) and bond characterization matrix implemented in the code, it is also implemented to introduce random structures in each generation during structural evolution. The elimination of similar structures in CALYPSO has greatly reduced the number of local optimizations, speeding up the global minimization convergence. The simulation is stopped when the halting criterion is reached.

1.4 Scope of the study

This study is focused on the prediction of new, stable structures and properties of functional solid crystals. These were carried out with Dr. Yansun Yao and members of Dr. M. Zhang's research group from the Department of Physics at the East China University of Science and Technology, Shanghai, China, and Dr. Huiyang Gou's group from the Centre for high pressure science and technology advance research, Beijing, China.

Chapter 2 focuses on the prediction of novel forms of single bonded nitrogen at high pressures. These predictions are performed using the metadynamics simulation [48] and the CALYPSO program [44] interfaced with the VASP code for structural optimization. Mechanical and dynamical stability was investigated at the DFPT level of theory as implemented in the PHONOPY program. In this study, we predict theoretically, and carefully characterize the newly found phase for single-bounded structure of nitrogen under extreme conditions. I, along with my supervisor, Dr. Yansun Yao and collaborators, predicted a new metastable structure and did relevant material properties calculations. I made key contributions by calculating the equations of state of the newly predicted and existing structures, investigated the dynamical stability (phonon

calculation) of the structures of interest and perform calculations to elucidate how the free energy as well as entropy of these structures changes with temperature.

Chapter 3 focuses on the prediction of the growth pattern of AlAu nanoclusters at ambient conditions. These predictions are performed using the CALYPSO program interfaced with the VASP code for structural optimization. Mechanical and dynamical stability was investigated using the displacement method as implemented in the PHONOPY program. In this study, to explore the growth pattern of Au_nAl_n (n=1-10) and carefully characterize the various stages of the growth process, I, along with my supervisor and collaborators, predicted the various structures with the lowest energy and did relevant material properties calculations. I contributed by calculating the energy dispersion (band structure), investigated the dynamical stability (phonon calculation) and performed calculation to elucidate the charge transfer mechanism in the stoichiometry (Bader charge analysis [49]) of the bulk phase of the cluster.

CHAPTER 2

A NEW SINGLE-BONDED HIGH-PRESSURE ALLOTROPE OF NITROGEN

2.1 Introduction

Nitrogen, under ambient condition is commonly found to be inert owing to the stable N≡N triple bond. Elemental nitrogen has been extensively investigated as a possible high-energy-density material (HEDM) under extreme conditions. Single bonded nitrogen network forms HEDMs in a metastable state due to the large energy difference between the single bonded network and a third of the triple bond. At low pressures and temperatures, nitrogen forms chemically inert and weakly interacting van der Waals solids consisting of triple-bonded N_2 molecules with great binding energy. This account for the stable nature of its crystal phases with characteristically large band gaps. It is not unexpected that the physical laws guiding this material may change at high pressures and temperatures because of the possibility of forming a more closely-packed phases at such extreme conditions. At extremely high pressures and temperatures, nitrogen can transform to single-bonded extended structures. This corresponds to molecular-to-nonmolecular solid transition. Due to a large amount of energy stored in the single bonds, the latter are efficient energy carriers, both in pure forms and compounds [50-53]. Allotropes formed solely by N−N single bonds could potentially be used as HEDMs, which are not only energy efficient but also environmentally friendly, producing only non-toxic N_2 during energy release. The single-bonded nitrogen was initially perceived to have the same crystal structures as isovalent black phosphorus (BP) or α-arsenic (A7), but in 1992, Mailhiot *et. al.* predicted a unique structure composed of fused

N_{10} rings connected in a way that all dihedral angles between N−N single bonds are in energetically favorable gauche helicity [54]. This 'cubic gauche (cg)' structure was later confirmed to be a thermodynamic ground state of nitrogen at high pressures [52]. In the last two decades, high-pressure structures of nitrogen have been extensively searched using various theoretical methods, which unveiled many interesting structures consisting of zero-, one-, two- and three-dimensional motifs, including larger molecules (0D) [55, 56], chains (1D) [57, 58], chaired webs (1D-2D) [59], layers (2D) [60], layered boats (2D-3D), and cages (3D) [61]. A theoretical high-pressure zero-temperature phase transition sequences appear to be acceptable, that is, from the molecular phase → cg → layered structure → cagelike structure in the gigapascal pressure region, and to a metallic salt structure at terapascal pressures. For example, Alemany *et al*. did an extensive theoretical study of nitrogen up to 500 GPa and found a phase transition of metallic form of nitrogen (0-20 GPa) to molecular diatomic nitrogen (20-27 GPa), then to the stable crystalline cubic *gauche* phase (27-205 GPa) and to the black phosphorous (BP) phase at pressures above 205 GPa [62-64].

Experimentally, a great amount of effort has been devoted to the synthesis of single-bonded nitrogen under extreme conditions. Early evidences of non-molecular nitrogen at high pressure were reported by several groups, while the realized structures were likely amorphous [65-67]. In 2004, the first crystalline form, the long-sought cg phase, at high pressure (>120 GPa) and high-temperatures (>2500 K), was successfully synthesized by Eremets *et. al.* [52]. Later, the cg phase was synthesized again at different pressure-temperature conditions [68-70]. In 2014, a new crystalline phase was synthesized above 120 GPa by Tomasino *et. al.* [53] which was thought to have a single-bonded structure as well. However, this new phase was found to mix with other phases (likely, amorphous and cg), making the structure identification challenging. The difficulties prevent a full-pattern Rietveld refinement of the experimental x-ray diffraction (XRD) data, but

the Le Bail profiling [53] suggests the structure is similar to a *Pba*2 structure predicted by Ma *et. al.*[63]. As such, the exact structure of this new phase is yet to be identified, which motivates the present study.

In this study, we determined the structures of this new phase through the application of first-principles metadynamics method. The *Pba*2 structure was found to be consistent with, but not sufficient to reproduce, the XRD pattern reported by Tomasino *et. al.* [53]. We proposed a new orthorhombic structure with the *Pccn* space group, which is energetically competitive with the *Pba*2 structure in the same *P*-*T* region of the synthesis. We also found that the simulated XRD pattern for the 1:2 mixture of the *Pccn* and *Pba*2 structures matches very well with the experimental data. In particular, several small 2θ angle peaks in the experimental XRD pattern are systematic absences in the *Pba*2 structure but can be satisfactorily explained by the *Pccn* structure. The *Pccn* structure is entirely single-bonded consisting of fused N_8, N_{10}, and N_{12} rings, as opposed to the *Pba*2 structure which has fused N_7 rings. The *Pccn* structure was found to be dynamically stable in the *P*-*T* region of the synthesis by phonon and vibrational free energy calculations.

2.2 Methods

The structures of the newly synthesized phase was predicted through the application of first-principles metadynamics method [48]. The *Pba*2 structure was deficient in reproducing the XRD pattern for the synthesized phase, most especially at small 2θ angles. Therefore, a new orthorhombic structure with the *Pccn* space group is predicted in this study, which is energetically competitive with the *Pba*2 structure in the stability pressure region of the synthesized phase. The internal and vibrational free energy for the *Pccn* structure was estimated at 140 GPa using the harmonic approximation in which all vibrational modes are treated as normal modes with the

frequency distribution described by phonon density of states. Phonons were calculated with a density functional perturbation theory (DFPT) method as implemented in VASP package [41,43], and using a 2×3×3 supercell as implemented in the PHONOPY [42] program for post processing. The Hellmann-Feynman forces and linear responses were calculated from the optimized supercell through the VASP package with a kinetic energy cutoff of 900 eV, and a 7×7×7 *k*-point mesh. A projector augmented wave (PAW) potential [17] with the PBE functional [71-72] were used. Convergence was achieved when the energy difference between two successive iterations was less than 10^{-6} eV per nitrogen atom. Metadynamics simulation was carried out in various simulation cells consisting of 32 to 96 nitrogen atoms with in the pressure range of 100 – 300 GPa, and in the temperature range of 1000-2500 K. The Gaussian width (W) and height (δs), related by $W \approx \delta s^2$were chosen to be 15 (kbar Å ^{3})$^{1/2}$ and 225 kbar Å ^{3}, respectively. A step length of 0.03 Å was employed for h-space sampling. The potential energy surface of N was searched up to 2000 metasteps. A finer *k*-spacing of 2π × 0.03 Å^{-1}was used in structural optimization and enthalpy calculations. First principles molecular dynamics (MD) simulations were performed at high temperatures for candidate structures using the VASP program, employing an isothermal-isobaric (NPT) ensemble with Langevin dynamics. Anharmonic vibrational density of states (*v*DOS) was obtained from the 20 ps MD trajectory (sampled with a 2 fs time interval) after 3 ps equilibrium time. To study the effects of changing temperature, the Helmholtz free energy at temperature T (0 - 2500 K) and volume V was calculated. The thermal electronic contribution to free energy [$F_{el}(V,T)$] is generally considered to be negligible away from melting point of the material hence vanishes. Thus numerical integration which is the sum over all phonon branches ω_λ in the first Brillion zone was carried. $\omega_\lambda(v)$ is the normal mode frequency of the phonon with polarization λ, evaluated at constant volume *V*, obtained from standard DFT calculation. Therefore,

$$F(V,T) = E_0(V) + F_{el}(V,T) + F_{vib}(V,T) \quad , \tag{2.1}$$

where $E_0(V)$ is the static contribution to the internal energy at volume *V* (also known as static crystal energy), which we also obtain from standard DFT (energy without entropy) calculation. Also,

$$F_{vib}(V,T) = k_B T \int_{\omega_\lambda} g(\omega_\lambda) ln\left\{2sinh\left(\frac{\hbar\omega_\lambda(V)}{2k_B T}\right)\right\} d\omega_\lambda \quad . \tag{2.2}$$

Putting $F_{el}(V,T) = 0$ and Eq. (2.2) into Eq. (2.1) yield:

$$F(V,T) = E_0(V) + k_B T \int_{\omega_\lambda} g(\omega_\lambda) ln\left\{2sinh\left(\frac{\hbar\omega_\lambda(V)}{2k_B T}\right)\right\} d\omega_\lambda \quad , \tag{2.3}$$

where $g(\omega_\lambda)$ is the density of states of each vibrational phonon frequency. Within the quasiharmonic approximation and for discrete phonon frequency, the vibrational free energy of a crystal can be approximated by

$$F_{vib}(V,T) = \frac{1}{2}\sum_{\omega_\lambda} g(\omega_\lambda)\hbar\omega_\lambda(V) + k_B T \sum_{\omega_\lambda} g(\omega_\lambda) ln\left[1 - exp\left(-\frac{\hbar\omega_\lambda(V)}{k_B T}\right)\right] , \tag{2.4}$$

and by extension, the free energy of a crystal is given by:

$$F(V,T) = E_0(V) + \frac{1}{2}\sum_{\omega_\lambda} g(\omega_\lambda)\hbar\omega_\lambda(V) + k_B T \sum_{\omega_\lambda} g(\omega_\lambda) ln\left[1 - exp\left(-\frac{\hbar\omega_\lambda(V)}{k_B T}\right)\right] \quad . \tag{2.5}$$

At $T = 0\ K$, the free energy reduces to the static contribution to the internal energy at volume *V*, colloquially known as the zero point energy (ZPE). The numerical integration shown (see later in

the discussion) in Fig. (2.11b) was normalized over the total DOS, $g(\omega_\lambda)$ according to $\frac{\int \omega_\lambda\, g(\omega_\lambda) d\omega_\lambda}{\int g(\omega_\lambda) d\omega_\lambda}$. To further understand the relationship between disorderliness, energy partitioning of fermions and temperature chages in the *Pccn* structure, we evaluate the entropy of the system according to

$$S(V,T) = \frac{(E_0(V) - F_{vib}(V,T))}{T} \quad , \tag{2.6}$$

where each symbol has conventional meaning.

The crystal-orbital Hamilton-population (COHP) and integrated crystal-orbital Hamilton population (ICOHP) analyses were performed using the LOBSTER program [73-75], taking into account all valence orbitals. Similar to the Crystal Orbital Overlap Population (COOP), the COHP analysis provides a quantitative measure of the bond strengths in crystals (-COHP values), where the positive and negative signs represent bonding and antibonding states, respectively.

2.3 Results and Discussion

2.3.1 Crystal structure and bonding of new and competitive N

The *cg* structure of nitrogen was adopted as the starting structure for the metadynamics simulation since the new phase reported by Tomasino *et. al.* [53] was synthesized at pressures above the stability field of the *cg* phase. The simulation searches for the low-energy transition pathways leading from the initial energy well (cg) to neighboring minima (new phases) in the potential energy surface, which enables the reconstruction of phase transitions. The present simulation revealed several high-pressure structures of nitrogen, including the previously proposed

BP, *C*2/*c*, [76] and *Pba*2 [63] structures, at different *P*-*T* conditions. The most interesting finding, however, is an orthorhombic *Pccn* structure discovered at 2500 K at pressures between 100 and 150 GPa. The transition mechanism between the cg and *Pccn* structures is illustrated in Figs. 2.1 (a) to 2.1(b).

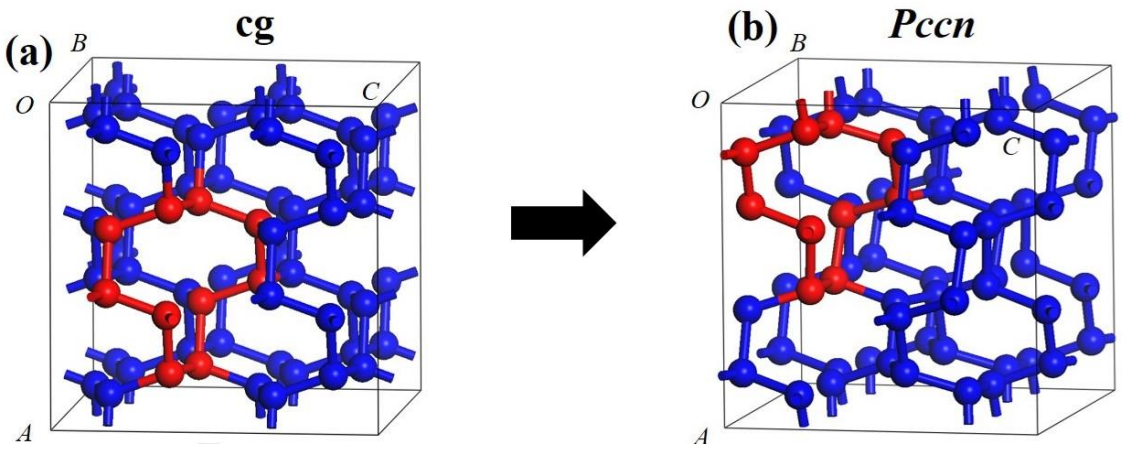

Figure 2.1. (a) The cg and (b) the *Pccn* structures. A N_8 ring is highlighted in red (shade) in each structure.

The *Pccn* is a purely single-bonded structure, in which each atom bonds to three neighbors and carries one lone-pair (*lp*) [Fig. 2.1(b)]. This structure is characterised by three types of ring structures, N_8, N_{10}, and N_{12}, fused together in a distorted tetrahedral sp^3 network as shown in Fig. 2.2.

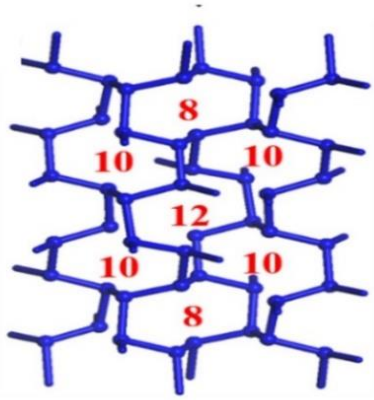

Figure 2.2. Construction of the *Pccn* structure by fused N_8, N_{10} and N_{12} rings.

Similarly, the cg structure is also single-bonded, but it contains only the N_{10} rings as shown in Fig. 2.3. The *cg* → *Pccn* transition is depicted in Fig. 2.4 (a) and (b). This implies that every second vertical array of the N_{10} rings in the cg structure breaks the bonds between the rings and creates new bonds to form a new array of alternating N_8 and N_{12} rings, while the other N_{10} rings keep the integrity but distort notably to accommodate the bonding changes.

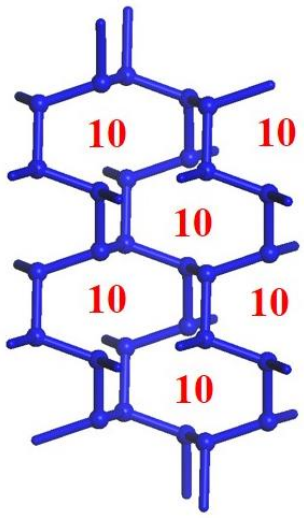

Figure 2.3. Construction of the cg structure by fused N_{10} rings.

The resulted *Pccn* structure loses '*all guache helicity*' but it is still an energetically favorable configuration. In the *Pccn* unit cell, 8 out of the total 48 dihedral angles (of *lp*-N-N-*lp*) have the *trans* conformation (see Fig. 2.5 b) where the *lp* repulsions are minimized [59, 77]. The rest 40 dihedral angles are all in the *gauche* conformation (see Fig. 2.5 a), and, of which, 20 are between 103.5° and 106.5°, similar to the *gauche* angles in the cg structure (~104.8°) [54], and 16 are at 90.6°, close to the *gauche* angle in H_2N-NH_2 (~91°) [78].

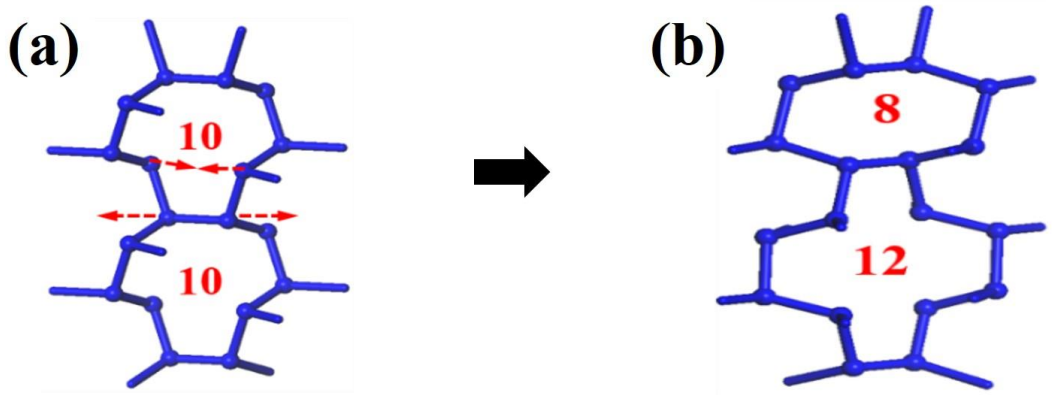

Figure 2.4. (a) and (b) Transition mechanism between an array of fused N_{10} rings to an array of alternating N_8 and N_{12} rings. Arrows in (a) indicate the bond breaking/forming directions.

The right-angle conformer (new allotrope gotten from right-angle rotation of the *gauche* angle about the single bond) is an energy minimum since it minimizes two-orbital/four-electron destabilizing interaction between the adjacent lone pairs. The other angles in the *Pccn* structure are 121.1° in nearly ideal staggered conformation. There are no energy maximum *cis* conformation in the *Pccn* structure. This configuration results in a distribution of the single bond lengths in the *Pccn* structure between 1.329 Å to 1.635 Å, as opposite to the unique bondlength (1.421 Å) in the cg structure.

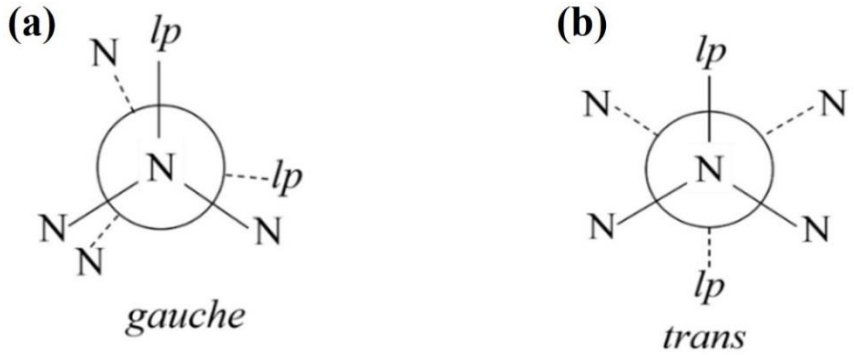

Figure 2.5. (a) and (b) Newman projections of *gauche* and *trans* conformers in solid nitrogen.

The strength of the single bonds in the *Pccn* structure was evaluated using the -COHP and -ICOHP analysis, and the results are compared with that of the cg structure as shown in Fig. 2.6. Clearly, a 'shorter bond = stronger bond' paradigm is revealed in the nearly linear relation between the integrated COHP values and the bondlengths, which seems to be independent of crystal structure (inset).

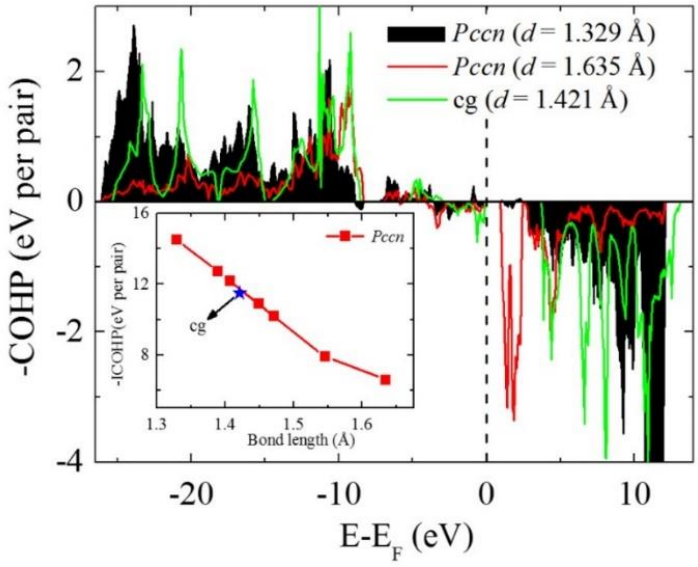

Figure 2.6. Calculated -COHP values for bonded N-N pairs in cg and *Pccn* structures. The shortest (1.329 Å) and longest (1.635Å) bonds in the *Pccn* structure were selected for presentation. Inset shows the ICOHP values for bonded N-N pairs in cg (1.421 Å) and *Pccn* (between 1.329 Å and 1.635 Å) structures.

The shortest bond (1.329 Å) in the *Pccn* structure has the largest -ICOHP value (14.52eV/pair), which sets up a favorable condition for mechanical stability, but the longer bonds go against it and compete. On average, the bond length in the *Pccn* structure is 1.461 Å (see Fig. 2.7), slightly larger than that in the cg structure (1.421 Å). The overall stability of the *Pccn* structure, therefore, is less than that of the cg structure.

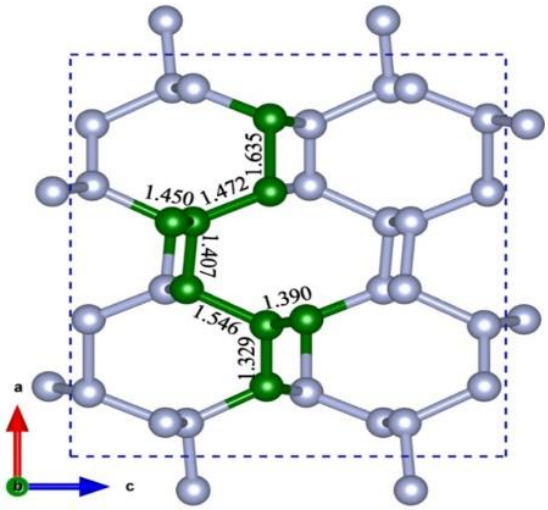

Figure 2.7. Distribution of N-N pairs in the *Pccn* structure, where atoms are colored in green to guide the eye.

The structural parameters of the *Pccn* structure (optimized at 137 GPa) are 8*e*: 0.1638, 0.8230, 0.5504; 8*e*: 0.6592, 0.6684, 0.5378; 8e: 0.4026, 0.4077, 0.2727; 8*e*: 0.9074, 0.2019, 0.2573, with a = 6.96 Å, b = 3.45 Å, and c = 6.84 Å. The experimental XRD pattern reported at the same pressure [53] was used to examine the structures. We found that none of the known theoretical structures alone is able to sufficiently reproduce the experimental XRD pattern, but the combination of the *Pccn* structure and the *Pba*2 structure predicted by Ma *et. al.* [63] (in 1:2 ratio) appears to be an excellent match as shown in figure 2.8.

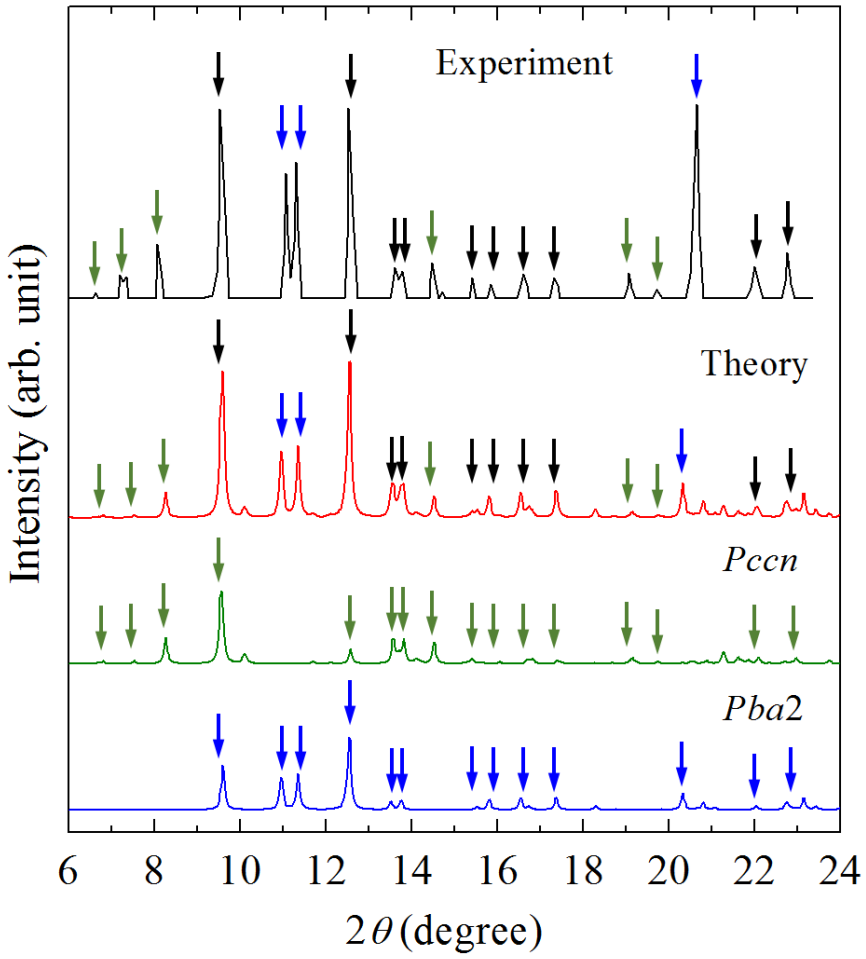

Figure 2.8 Calculated XRD patterns for the *Pccn* structure, the *Pba*2 structure, and the 1:2 mixtures of the two structures at 137 GPa, compared with the experimental XRD pattern at the same pressure. The experimental XRD pattern was adapted from Ref. 53. Copyrighted by the American Physical Society.

This confirms that the synthesized phase is a multi-phase mixture. The simulated XRD pattern reveals that the majority of the observed Bragg peaks belongs to the *Pba*2 structure. The two peaks at 10.9° and 11.3° can be uniquely indexed to the *Pba*2 structure, while the two at 9.5°, and 12.2° appear to be overlapping with the peaks from the *Pccn* structure. The two peaks at 8.3° and 14.3° are signature peaks of the *Pccn* structure, which are indexed to (111) and (121),

respectively. The weak peaks below 8° and those between 19° and 20° can also be uniquely indexed to the *Pccn* structure. Essentially, most of the 2θ positions of the Bragg peaks can be successfully matched to the experimental XRD. The relative intensities of the peaks however have a various degree of deviation, in particular for the peak at 20.2° ((213) of the *Pba*2 structure). This could be due to a slight modification of the structure and the preferred orientation of the crystal. It should also be noted that due to the experimental difficulties, such as weak x-ray scattering of nitrogen and the uncertainties in the background subtraction, the present experiment-theory comparison shows a consistency that supports the presence of the *Pccn* and *Pba*2 structures but this does not rule out the possibility that other structures, such as the *C*2/*c* [76] and cg [54] structures, may co-exist in this *P*-*T* region.

2.3.2 Equations of state and dynamical stability

The enthalpies of the candidate structures of nitrogen ($H = E + pV$) are compared in Fig. 2.9 over the pressure range 100-300 GPa. This comparison includes the *Pccn* structure and several previously predicted structures (cg, BP, *Pba*2, $P2_12_12$, $P\text{-}42_1/m$ [14], and *C*2/*c*). The cg and *Pba*2 structures were found to be the lowest enthalpy structure below and above 190 GPa, respectively, which agrees well with previous calculations [61, 63-64]. In the 100-140 GPa range, both the *Pccn* and *Pba*2 structures have higher enthalpies than the cg structure. This indicates that they are not thermodynamic ground state at 0 K but could be metastable at high temperatures as we will find out later in this discussion. The experimental observation of the new phase at high temperatures, *i.e.*, above 2500 K, appears to support this conjecture. At 120 GPa, the enthalpy differences between these two structures and the cg structure are about 0.07 and 0.1 eV/atom, respectively, which, in term of equivalent temperature, are 812 K and 1160 K. In this pressure range the

previously predicted *C*2/*c* structure [76] is also energetically competitive, and therefore could also be a candidate structure. For other structures, since their simulated XRD patterns do not correspond to the experimental observations, they are not considered further. The dynamical stability of the *Pccn* structure is established by the phonon calculations as shown in Fig. 2.10. The absence of imaginary frequency in the phonon dispersion relations confirms the stability of the *Pccn* structure. Notably, the optical branches are nearly flat revealing non-dispersive N-N vibrons in the ring structures. Due to the particular vibrational modes, one expects that the *Pccn* and cg structures have different vibrational internal energy U_{vib} and free energy F_{vib} that could compensate for the enthalpy difference.

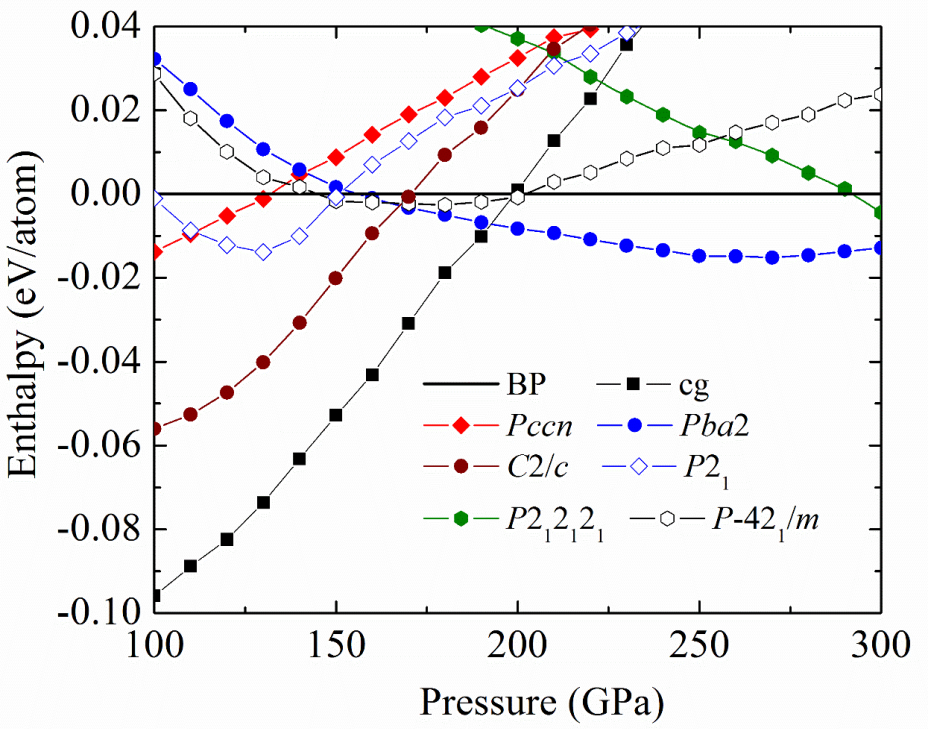

Figure 2.9. Enthalpies as functions of pressure for candidate structures of high-pressure nitrogen. The enthalpy of the BP structure is used as the zero-energy reference level.

To this end, we estimated the U_{vib} ($-\partial ln(Z)/\partial\beta$) and F_{vib} ($-ln(Z)/\beta$) for the *Pccn*, *Pba*2 and cg structures at 140 GPa using the harmonic approximation [72] in which all vibrational modes

are treated as normal modes with the frequency distribution described by actual vibrational density of states (*v*DOS). The *v*DOS was calculated at five different temperatures between 500 and 2500 K using single-particle velocity autocorrelation function obtained from the thermal trajectory of a 20 ps NPT molecular dynamics simulation, which captures both harmonic and anharmonic vibrations [79]. Fig. 2.11(a) exemplifies the *v*DOS of the *Pccn* structure at three temperatures, compared with the phonon DOS at 0 K. Clearly, the overall profile of the *v*DOS is retained at high temperatures even up to 2000 K.

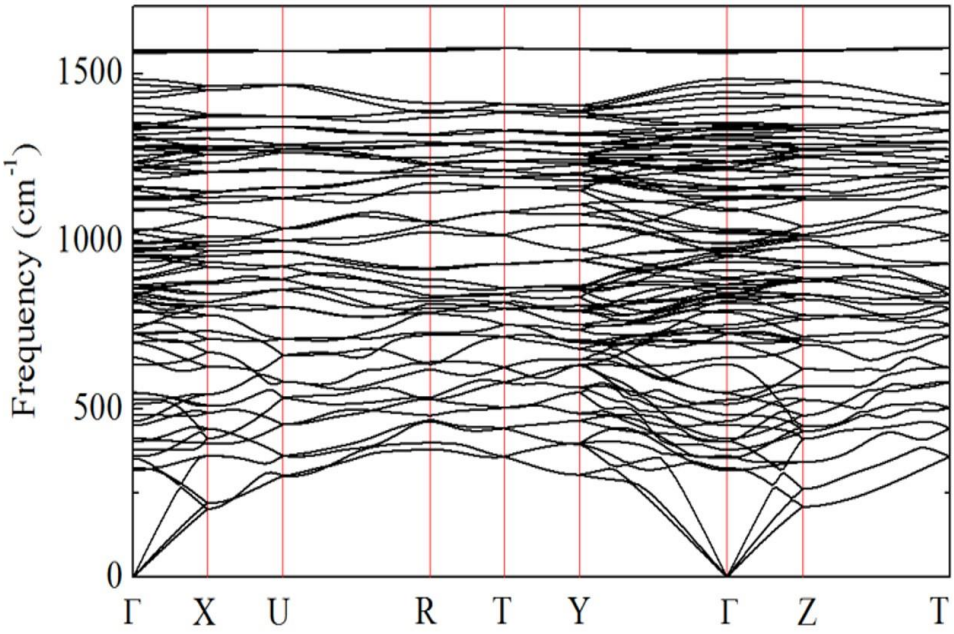

Figure 2.10. Phonon dispersion relations for the *Pccn* structure at 140 GPa.

Compared with phonon DOS, the *v*DOS at finite temperatures have broadened peaks due to greater degrees of freedom, and slightly lowered frequencies due to the unit cell expansion. The calculated energy sum $H + U_{vib}$ and $H + F_{vib}$ for the *Pccn*, *Pba*2 and cg structures at 140 GPa are illustrated in Fig. 2.11(b) as functions of temperature. Here the enthalpy values (H) are taken from the static calculation (Fig. 2.9). Taking into account, the zero-point contributions, at T = 0 K the

cg structure is more stable than the *Pccn* and *Pba*2 structures by -0.052 and -0.053 eV/atom, respectively [Fig. 2.11(b)]. When raising the temperature, the internal energies U_{vib} of all structures increase, but the differences of U_{vib} between the structures are nearly constant, signifying the energy equipartition in this temperature regime. The relative stability of the structures is therefore determined by the entropic contributions to the F_{vib}, or $-TS_{vib}$. The F_{vib} are notably lower in the *Pccn* and *Pba*2 structures than in the cg structure, suggesting that a phase transition might occur as a consequence of the increased entropies at sufficiently high temperatures (but below the melting point).

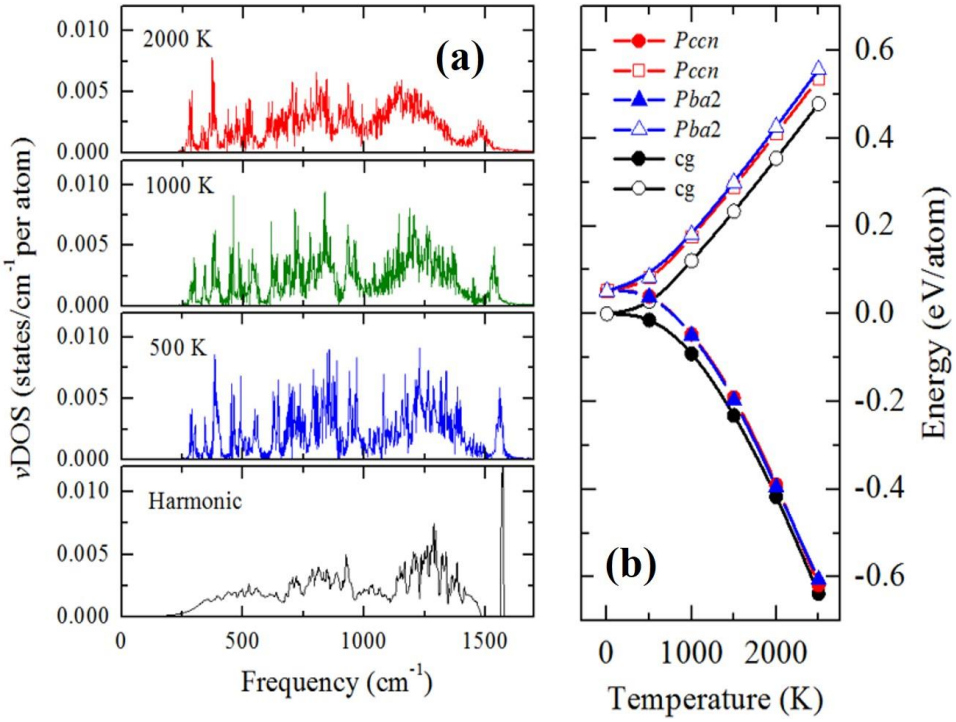

Figure 2.11. (a) Phonon DOS and temperature-dependent *v*DOS for the *Pccn* structure at 140 GPa. (b) The temperature-dependent $H + U_{vib}$ (open symbols) and $H + F_{vib}$ (solid symbols) for the *Pccn*, *Pba*2 and cg structures at 140 GPa (see text). The energy of the cg structure at 0 K was used as the zero-energy origin.

As shown in figure 2.11(b), the $H + F_{vib}$ curves bend down, and their differences decrease at high temperatures, suggesting the *Pccn* and *Pba*2 structures to become more stable with increasing temperature. With the F_{vib} accounted, the *Pccn* and *Pba*2 structures are only higher in energy than the cg structure by -0.019 and -0.032 eV /atom, respectively, at 2500 K. Given a small energy deficiency, the *Pccn* and *Pba*2 structures may therefore be stabilized by kinetics at high temperatures, utilizing the high mechanical stability of the sp^3 covalent networks.

2.4 CONCLUSION

In conclusion, we report a new single-bonded structure of nitrogen at 2500 K at pressures between 100 and 150 GPa which is likely to be a part of the newly synthesized polymeric nitrogen phase in the same *P*-*T* region. The predicted *Pccn* structure is composed of fused N_8, N_{10}, and N_{12} rings connected in a way that all *lp*-N-N-*lp* dihedral angles are in low-energy *gauche* or *trans* conformations. The simulated XRD pattern of a mixture of the *Pccn* structure and a previously proposed *Pba*2 structure matches the experimental data very well. Dynamical stability of the *Pccn* structure is established by phonon calculations which reveals no imaginary frequencies in the entire Brillouin zone. Vibrational free energy calculation utilizing the temperature-dependent *v*DOS obtained from molecular dynamics simulations shows that the *Pccn* structure is marginally higher in energy than the cg structure (~ 0.02 eV/atom) at 140 GPa and 2500 K, indicating that the structure is stabilized by kinetics. The present study establishes another single-bonded nitrogen phase after the lab-synthesized cg phase and advances the understanding of the phase diagram of nitrogen under extreme conditions, which will stimulate the study of metastable phases of nitrogen for energy storage applications.

FUTURE WORK

In the future, I will like to push this project little further by exploring the experimental confirmation of some existing and newly predicted phases of nitrogen. This work is already in progress. This is anticipated to further establish reliability of various theoretical models and methods employed in this thesis and push the frontier of research on HEDMs.

CHAPTER 3

GROWTH MECHANISM OF BIMETALLIC NANOALLOY CLUSTERS: Al_nAu_n (n=1-10)

3.1 Introduction

Clusters often exhibit unique properties different from those of individual atoms and bulk materials. The discovery of fullerene C_{60} and its variations [80] represents the first appearance of functional clusters in materials research, which, has since that time stimulated great enthusiasm. In recent years, scientists have shifted the direction of their research to understand the growth mechanism of systems from cluster to their solid-state forms. This is expected to open an avenue for property tweaking and manipulation for technological applications. The solid-state manifestation of fullerenes, fullerites, for example, can be processed to a nanocrystalline ultrahard form which has growing applications in armor.

Lowest-energy structures for Au_n species or alternative configurations has been intensely searched and studied partly due to the phenomenological D_{3h} isomer stabilization which has been linked to the spin-orbit coupling effects. Gold nanoclusters spikes the interests of present-day research due to their applications in optoelectronics and catalysis. As opposed to the inert bulk form, gold clusters (or nanoparticles) have enhanced catalytic activity which was found to be strongly correlated with the structures. Over the years, structures of small gold clusters (< ~32 atoms) have been well established [81-97]. Previous studies have unveiled different structural configurations preferred by Gold nanoclusters in their stable forms. They were found to range from 2-D planar to 3-D cage- and tube-like structures [98-102]. Hinged on strong relativistic effects

which leads to metal–metal interactions, [103] gold clusters can be doped with other metals, forming bimetallic clusters, where aluminum is considered as a prominent dopant, partly due to its abundance, characteristic electronic shell closing and simultaneous occurrence of several geometries. Although being a nearly free electron metal, aluminum has particularly different behaviors in low dimensions which lead to its use as a dopant element. Some particular aluminum clusters, colloquially known as 'superatoms' have been found to behave similar to the halogen, alkaline earth, and other multivalent species [104-108].

As such, the structures and properties of bimetallic Al-Au cluster have been actively investigated. While emphasis of past studies has been primarily focused on the Au-rich side [109-116], the Al-Au equal or Al-rich clusters in this group have been relatively less explored. Just recently, the neutral and anionic Al_2Au_2 clusters were discovered, by a combined photoelectron spectroscopy (PES), high-resolution photoelectron imaging, and first principles study [117]. This can be considered a bold step in the direction of extending the Al-Au clusters toward the Al-rich side. Shortly after, a series of Al-rich Al-Au clusters has been found, with the composition $Au_xAl_y^-$ ($x+y = 7,8$; $x = 1–3$; $y = 4–7$) [118]. Motivated by these new findings, theoretical study and exploration of the possibility of expanding the new Al_2Au_2 cluster, where the Al and Au have equal composition, to a larger cluster size, and to an extended crystalline phase was investigated in this study. The goal is to rationalize the growth mechanism from the cluster to crystalline phase in this new family which hopefully can lead to new discovery in nanomaterials design and fabrication. To this end, prediction of thermodynamic ground geometries of the Al_nAu_n clusters up to 20 atoms, as well as the solid state structure of crystalline AlAu, using an *ex nihilo* structure search methodology based on particle swarm optimization (PSO) algorithm was carried out. The size-dependent structural characteristics from clusters to crystal were rationalized, coupled with a

discussion of the various structural motifs believed to have originated from different bonding strategies. Finally, a proposal of a new building block for nanomaterials composed of Al and Au, and analysis of the convergence of cluster properties toward the corresponding bulk values are presented.

3.2 Methods

The potential energy surface of AuAl non-periodic system was extensively searched for candidate structures of Al_nAu_n clusters using the CALYPSO method, which has been proved to be an efficient method for cluster structure prediction [44, 119-120]. The CALYPSO method implements particle swarm-intelligence optimization (PSO) algorithm during potential energy surface exploration for non-periodic systems [120], combined with structure optimization using Gaussian package with PBEPBE/LANL2DZ basis set. More than 3000 distinct isomers (local energy minima) were selected from the energy surface for finer optimization using all-electron spin-unrestricted calculation with the $DMOL^3$ program, [121-122] and the Perdue-Burke-Ernzerhof (PBE) functional. Relativistic calculations were carried out with scalar relativistic corrections to valence orbitals, *i.e.*, orbitals that participate in bonding, *via* a local pseudopotential (VPSR) employing double numerical plus polarization with addition of diffuse functions (DNP+). Convergence of self-consistent field (SCF) was set with a criterion of 1×10^{-5} Hartree on total energy and electron density, 2×10^{-3} Hartree/Å on the gradient, and 5×10^{-3}Å on the displacement. Harmonic vibrational analysis was carried out at the same level of theory to examine the stability of low-energy isomers and estimate zero-point energy (ZPE) corrections.

Crystalline AlAu structures were also obtained using the CALYPSO method and fully optimized using CASTEP package [123] and PBE functional, with the van der Waals corrections [124-125] included for treating the dispersion interactions. Brillouin zone integration was carried out on a 10×10×1 Monkhorst−Pack *k*-points mesh in geometry optimizations along with a kinetic energy cutoff of 600 eV. Phonons were calculated with a displacement method using a 2×3×3 supercell as implemented in the PHONOPY program. The Hellmann-Feynman forces were calculated from the optimized supercell through the VASP package [41] with a kinetic energy cutoff of 500 eV, and a 7×7×7 *k*-point mesh. A projector augmented wave (PAW) potential with the PBE functional were used. Convergence was achieved when the energy difference between two successive iterations was less than 10^{-6} eV.

3.3 Results and Discussion

3.3.1. Structures of Al_nAu_n Clusters and Crystalline AlAu

The Al_nAu_n clusters with equal Au and Al compositions have more diversity in structures than singly doped $AlAu_{2n-1}$ or $Al_{2n-1}Au$ clusters which can analogously be compared to the task of choosing equal number of heads and tails from a group of coins. Apparently, the task is more complex than choosing only one. Prediction of the ground-state and metastable structures of Al_nAu_n isomers up to n = 10 using the swarm-intelligence structure search have been done. The representative results are presented in Fig. 3.1, with the structures ordered according to the number of Au and Al atoms forming the cluster.

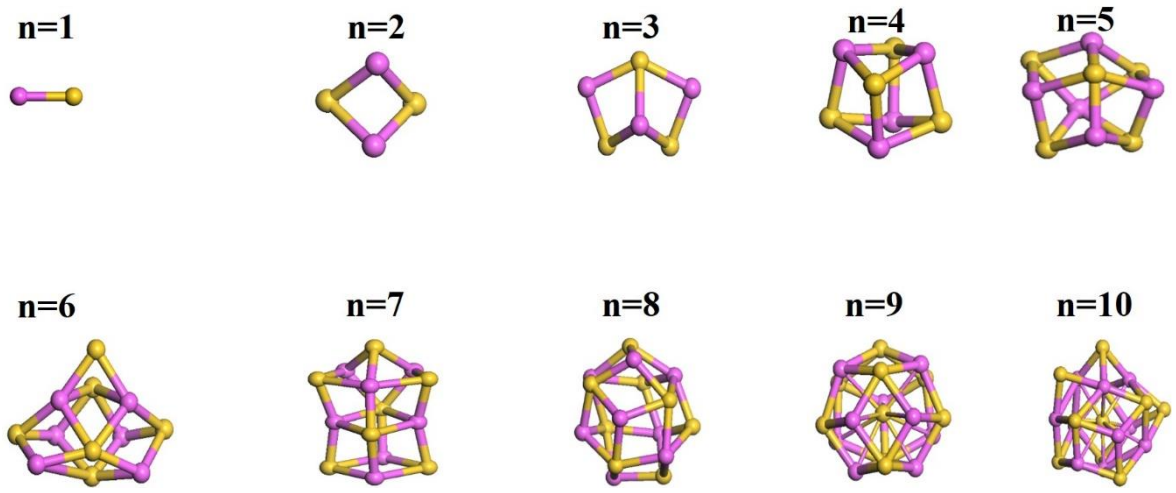

Figure 3.1. Crystal structures of representative cluster for n=1-10. Each figure represents the lowest enthalpy structure for the given stoichiometry [126].

An interesting feature of the ground state geometries of neutral Al_nAu_n clusters is that all clusters prefer three dimensional structures (see Fig. 3.1). Such preference can be traced to the strong and favorable Al-Au interactions developed within the cluster. In the cluster environment, electrons tend to transform from Al to Au due to a greater electronegativity of the Au, forming nominal $Al^{\delta+}$ and $Au^{\delta-}$. Thus, the Al-Au interactions are energetically favorable, stabilizing the clusters by strong electrostatic attractions, and thereby facilitating the growth of the clusters. It is not surprising that all the ground-state Al_nAu_n clusters have closed structures with alternating arrangement of Al and Au atoms which maximize the Al-Au interactions. In addition, this bonding strategy also minimizes unfavorable Al-Al repulsions as Al has high metallicity. In contrast, pure Au_n clusters were predicted to have two dimensional, close-packed, planner structures until *n* reaches 13, which is primarily due to strong relativistic effects as shown in Fig. 3.2.

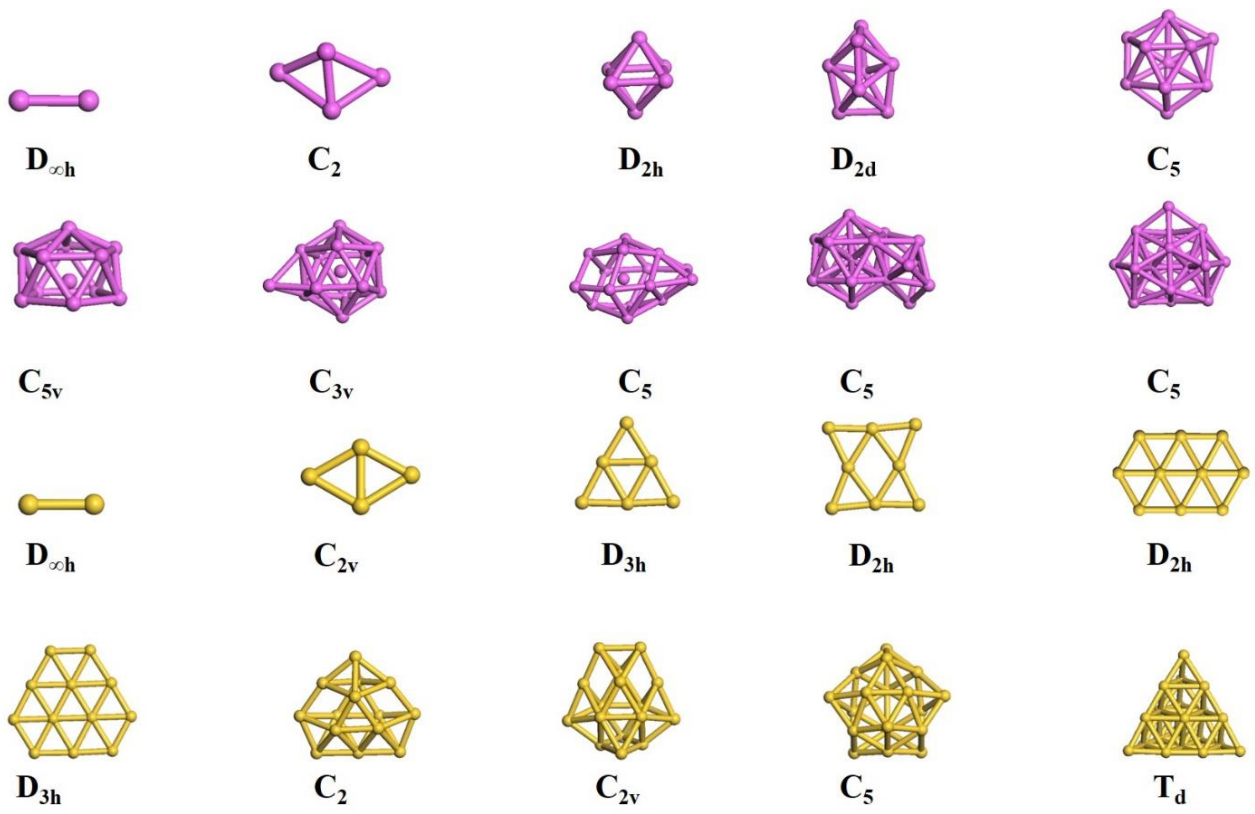

Figure 3.2. The lowest-energy structures of the corresponding bare Al_{2n} and Au_{2n} (n=1-10) clusters. Pink and yellow circles represent gold and aluminum atoms, respectively [126].

The two dimensional Au clusters have previously been synthesized, for example, on insulating self-assembled monolayers (SAM's). Pure Al_n clulsters, on the other hand, favors three dimensional networks. The predicted ground-state geometries of Al_n and Au_n clusters are in good agreement with the previous studies [82-84,98,127-129].

In detail, the diatomic AlAu has a $C_{\infty v}$ symmetry with the calculated average vibrational frequency of 9.97 THz, which is in excellent agreement with the experimental results of 9.99 THz

[114]. The ground-state geometry of the Al_2Au_2 cluster has a four-member ring structure with the C_{2v} symmetry, which is identical to the experimentally identified structure by high-resolution PES [117]. Another way of looking at the C_{2v} structure is a closed ring of alternating Au and Al. It can be explained that a 'closed' structure is likely more stable than an 'open' structure due to favorable Al-Au interactions that the closed configuration tends to maximize. The argument goes back to the simplest ring structure, H_3^+, which clearly prefers equilateral triangle geometry to an open chain. In fact, as it is shown in figure 3.1, all the predicted Al_nAu_n clusters in this work prefer closed structures.

The predicted ground-state geometry of Al_3Au_3 has a book structure (see Fig. 3.1). Like with the diatomic cluster, this geometry is suited to maximize the Al-Au interactions. Other isomers, such as rectangle (C_1), benzene analogue (C_{3v}) structure, or distorted triangular structures, either have less Al-Au interactions or have unfavorable Al-Al interactions, leading to higher energies. From n = 4 to 9, the Al_nAu_n clusters adopt closed, cage-like structures. The predicted ground-state Al_4Au_4 cluster has a square antiprism with D_{2d} symmetry. Such a structure yields maximum twelve Al-Au bonds, forming a closed cage. Similar cage structure has previously found in VCs_8, VNa_8, and VLi_8 clusters, where the alkali metal form cages (so called 'superatoms') with dopant V atom situated in the center [130-132]. The hollow cage structures from Al_4Au_4 to Al_8Au_8 are facilitated by the same bonding strategy, but the Al_9Au_9 has a filled cage structure with one Au atom in the center in order to maximize its Al-Au interactions with successive gold atoms surrounding the central aluminum site (the bond of ambient Au and the center Al are depicted with thin stick radius in Fig.3.1). This situation is similar to the high stable $W@Au_{12}$ cluster, which has a highly symmetric icosahedral structure with the 5d tradition metal atom W encapsulated in the Au_{12} cage having particularly efficient radial bonding [133-134]. At n = 10, the cluster adopts a three

dimensional network, showing the onset of periodicity and the characteristics of an extended crystalline structure.

The Al_nAu_n becomes a crystalline phase when n approaches infinity. To this end, we also searched for the stable crystalline AlAu structures with the swarm-intelligence structure search method. The predicted ground-state crystalline phase has a monoclinic unit cell with the $P2_1/m$ space group (Fig. 3.3), which is very close to the experimentally known geometry of this structure within the accuracy of the DFT method (Table 3.1) [135-136].

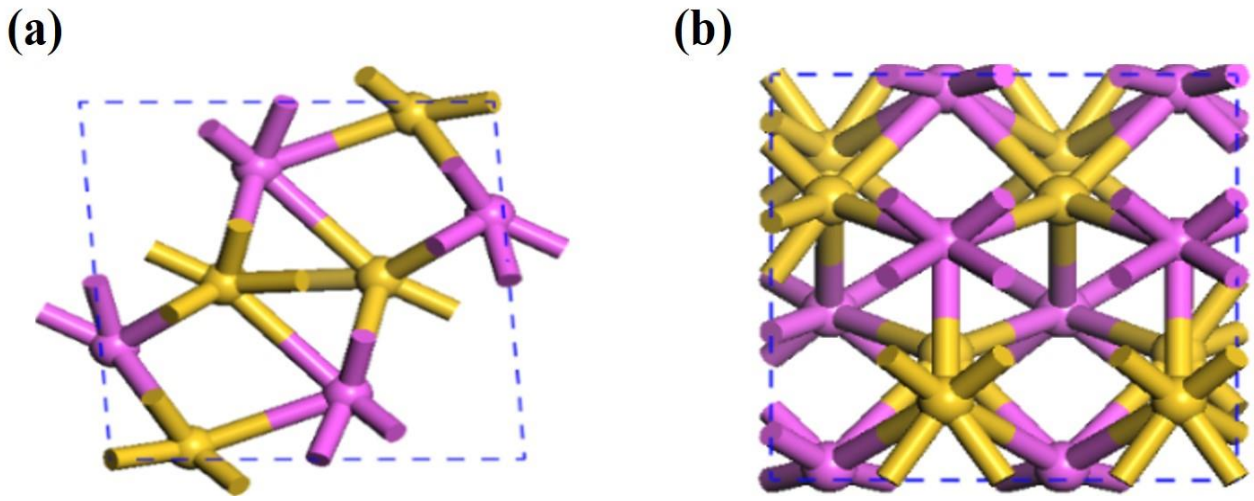

Figure 3.3. Optimized crystal structures of Al-Au bulk phase from the top view (left) and the side view (right). Crystal structure data for these structures are listed in Table 3.1[126].

System	SG	a	b	c	α	β	γ	Δ E (eV)
Expt.	_	6.399	3.333	6.325	90	93.14	90	_
	_	6.405	3.333	6.327	90	92.99	90	_
Fig. 3.2	$P2_1/m$	6.51	3.28	6.38	90	94	90	0

Table 3.1. The symmetry group (SG), lattice parameters of lengths (Å), angles (degrees) and the relative energies of ΔE per cell (in eV) with respect to the most stable structure for the Al-Au bulk phase depicted in Figure 3.3 [126].

This structure can be viewed as a monoclinically distorted NiAs structure for AB alloys, with the coordination numbers for Al and Au increased to 8 and 9, respectively. Interestingly, a common feature shared by the crystalline AlAu and aforementioned Al_nAu_n clusters is the existence of an Al_2Au_2 tetrahedron (four member ring), which may be considered as the 'building block' for the structural growth as shown in Fig. 3.4. All Al_nAu_n clusters, from n = 1 to 10, can be viewed as low-energy edge-sharing arrays of the Al_2Au_2 units. In the crystalline phase, the trace of Al_2Au_2 motif is also clearly visible (highlighted by dotted ecliptics, Fig. 3.4).

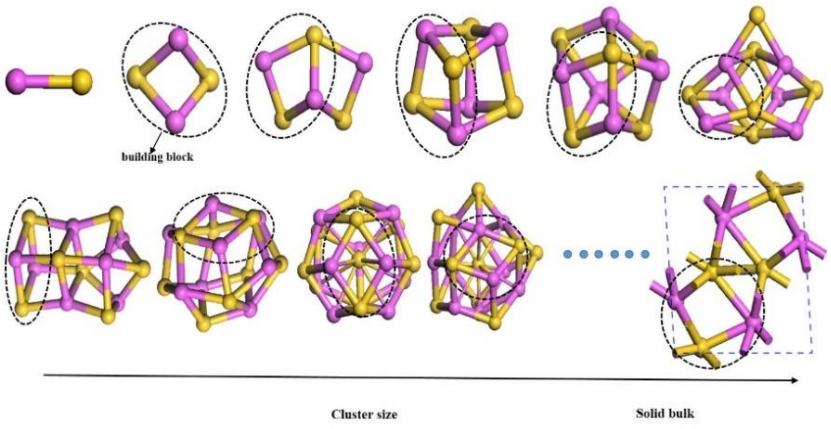

Figure 3.4. Structural evolution from the neutral Al_nAu_n (n=1-10) clusters towards crystal structure. Pink and yellow circles represent aluminum and gold atoms, respectively [126].

3.3.2. Electronic Structures

Various types of standardized analysis were done to characterize the electronic structure and properties of various cluster sizes predicted up to the crystalline phase. To visualize the Al-Au interactions in Al_nAu_n, we have demonstrated the deformation electron density (DED), defined as the difference between the charge density of the cluster and the charge density sum of individual atoms. Using Al_4Au_4 and Al_5Au_5 as examples, the DED are analyzed in figure 3.5. In both clusters, electron accumulation is clearly revealed around midway of the Al-Au contacts, showing covalent characteristics. Yet, there is a substantial charge transfer from Al to Au due to the greater electronegativity of the Au, which facilitates polarized Al-Au interactions.

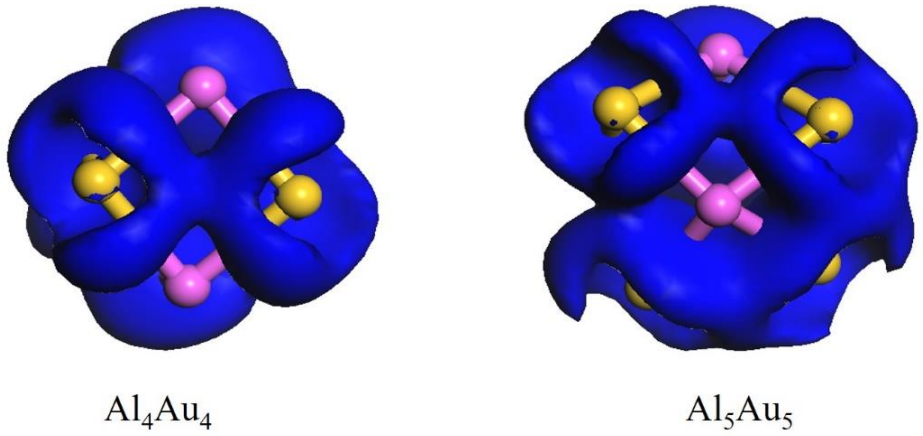

Figure 3.5. The deformation electron density (DED) of the Al_4Au_4 and Al_5Au_5 clusters. Charge accumulations are obvious in blue regions. The surface isovalue for electron density is 0.03 e/Å^3 [126].

Clearly, in all clusters the Au atoms are anionized, gaining fraction of electron ranging from 0.35 ~ 0.57 e^-/atom. It should be noted here that, although being an inert element, Au is easily

anionized in alloys and solid solutions. Bader Charge Analysis was done on the crystalline AlAu revealing that each Al atom (s^2p^1) transferred electron to the corresponding Au atom (s^1d^{10}) in the unit cell as shown in Table 3.2. Thus, in the stoichiometry of AlAu crystal, the result of the Bader charge analysis clearly shows that Au will be anionic while Al will be cationic in their configurations. Au atoms are anionized by gaining a whole and some fraction of electron ranging from ~0.67 to ~ 0.68 e^-/atom, thereby behaving like its cluster configurations. The result of bader charge analysis is shown in table 3.2

S/N	Atom	Bader Charge (e)	Bader Charge transfer (e)
1	Au	12.68	-1.68
2	Au	12.67	-1.67
3	Au	12.679	-1.68
4	Au	12.67	-1.67
5	Al	1.35	1.65
6	Al	1.30	1.70
7	Al	1.35	1.65
8	Al	1.30	1.70

Table 3.2. Bader charge analysis on each atom in the crystalline AlAu unit cell.

The result of energy dispersion calculation shows that in extended AlAu structure, the bonding and antibonding orbitals form valence and conduction bands, respectively, which overlap near the Fermi level, leading to a metallic state. The kinetic stability of Al_nAu_n clusters is examined by the energy gap (E_{gap}) between the highest occupied molecular orbital (HOMO) and the lowest unoccupied molecular orbital (LUMO). The calculated energy gap of Al_nAu_n clusters which decreases with odd-even oscillation, as shown in Table 3.3, eventually vanishes in the crystalline AlAu phase (see Fig.. 3.6).

System	E_b	E_{gap}
Al_1Au_1	1.96	2.466
Al_2Au_2	2.51	1.963
Al_3Au_3	2.72	1.541
Al_4Au_4	2.87	0.717
Al_5Au_5	3.07	0.961
Al_6Au_6	3.10	0.624
Al_7Au_7	3.19	0.718
Al_8Au_8	3.24	0.33
Al_9Au_9	3.31	0.255
$Al_{10}Au_{10}$	3.37	0.461

Table 3.3. The average binding energies per atom (E_b) and the HOMO−LUMO energy gap (E_{gap}), of the Al_nAu_n (n=1-10) clusters for the lowest-energy structures.

Clearly, the odd-even oscillation of E_{gap} is due to the unpaired electrons in these particular clusters which reduces the HOMO-LUMO gap.

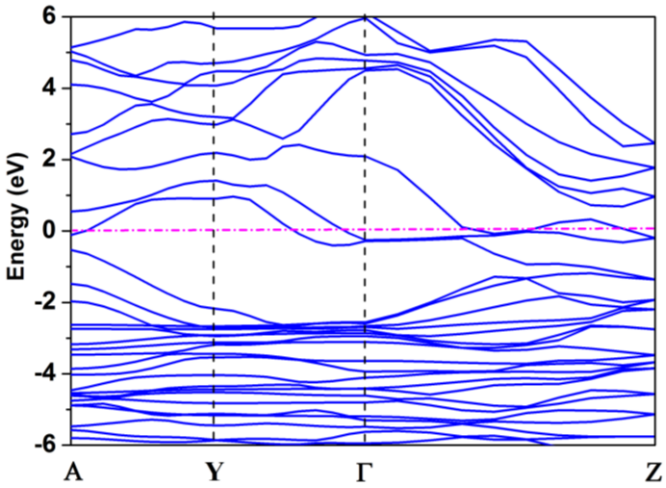

Figure 3.6. The band structure of the $P2_1/m$ structure. The horizontal dash-dot lines indicate the Fermi level [126].

In extended AlAu structure, the bonding and antibonding orbitals form valence and conduction bands, respectively, which overlap near the Fermi level, leading to a metallic state as shown in Fig. 3.6. The dynamic stabilities of Al_4Au_4 and Al_5Au_5 clusters and crystalline AlAu were tested using molecular dynamics simulation implemented in the CASTEP code at room temperature (T = 300 K). The NHL thermostat was used for NVT molecular dynamics. Within the employed simulation time of 2 ps, no structural changes were detected in any structure.

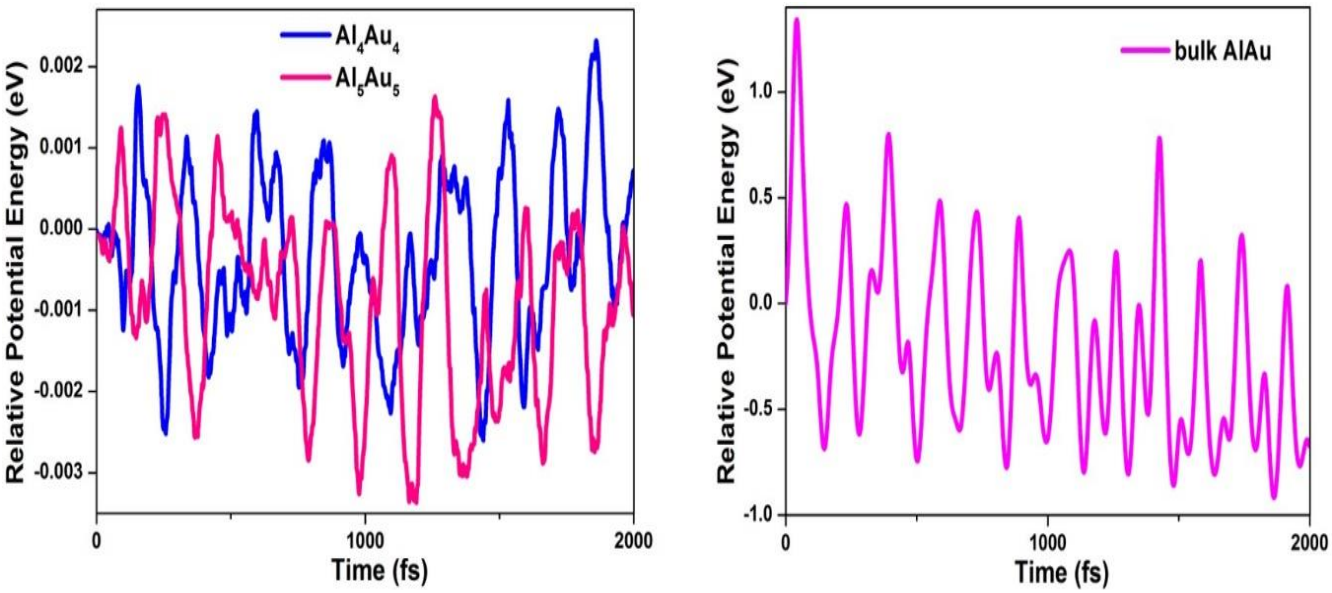

Figure 3.7. Relative potential energy (eV) of the Al_4Au_4 and Al_5Au_5 clusters (a), and Al-Au bulk for the lowest-energy structures during 2 ps of molecular dynamics simulation [126].

As seen in Fig. 3.7, the instantaneous values of the relative potential energy fluctuate due to thermal fluctuations but the average values stay constant. Thus, the ground-state clusters are expected to be stable at room temperature.

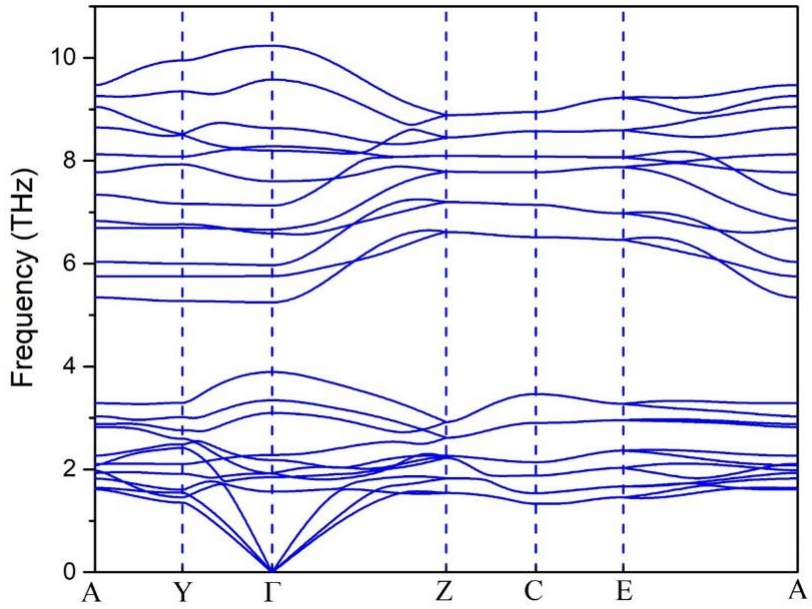

Figure 3.8. The Phonon dispersion relations of the $P2_1/m$ structure at ambient condition [126].

In addition, phonon dispersion relations of the crystalline AlAu phase were also calculated to investigate its dynamical stability. The result is as shown in figure 3.8. Notably, none of the vibrational modes contains imaginary frequency, suggesting that this structure is dynamically stable at ambient conditions.

3.4 CONCLUSION

In conclusion, the size-dependent structural and electronic properties of bimetallic Al_nAu_n (n=1-10) clusters have been systematically investigated by using relativistic all-electron density functional theory. A theoretical evidence is provided that points to the fact that Al_2Au_2 cluster can be used as the building block to construct the other Al_nAu_n clusters with successive Al and Au atoms, which can be used to probe the growth mechanism for cluster-assembled nanomaterials. It is further shown that this trace of Al_2Au_2 motif is also clearly visible in the bulk state. Since properties of nanomaterials depend on their size and shape, this work show the bottom-up approach

of nanoscience and provide a new way to discover the physical and chemical properties of such materials that are employed in physical processes like catalysis.

FUTURE WORK

In the future, I will like to push this project little further by theoretically predicting other cluster structures that are application driven. Various theoretical tools like the genetic algorithms and particle swarm-intelligence optimization algorithms under different implementations would be employed to predicts cluster structures targeted towards catalysis and other physical processes.

CHAPTER 4

CONCLUDING REMARKS

Interests in EMs research has experienced tremendous surge in the past years due to the peculiar ability of this class of materials to store relatively large amount of energy that are readily deliverable. Nitrogen is particularly interesting because of its abundance and 'environment-friendly' nature. It has been reported that high energy is stored in the single bond of nitrogen, which is released during bond rearrangement. This rearrangement of bond could be triggered by subjecting molecular nitrogen to extreme *P-T* conditions. Allotropes formed solely by N-N single bonds could potentially be used as HEDMs.

Furthermore, current technological innovations are driven by nanomaterials due to the need for miniaturization of various electronic and technological gadgets. This need has in a way caused rigorous investigation into the phenomenon of catalysis as it assists in efficient and cheap synthesis of functional materials. Clusters made of two metallic elements has been extensively studied and reported as a possible class of material suitable for catalysis for which Au_xAl_y (x,y are integers) clusters were specifically proposed. Most of the experimental as well as theoretical research done on this material has always favoured the Au rich side in the Au_xAl_y configuration. However, systems that are Al-rich or composed of equal proportion of both metals has been scarcely explored.

Motivated by the above backgrounds, a theoretical XRD study, combined with a range of theoretical thermal analysis techniques has been applied to study our newly predicted single-bonded nitrogen using PSO and metadynamics algorithm. This work has established that the newly

synthesised single-bonded nitrogen reported by Tomasino *et al.* [53], could in fact be a mixed phase of the previously predicted *Pba2* phase by Ma *et al.* [63] and the newly predicted orthorhombic structure with the *Pccn* space group reported in this study. The results of dynamic and thermal analyses show that at a very high pressure (> 120 GPa) and high temperature (> 2500 K), the new *Pccn* structure could become more stable and energetically more favourable than the previously reported phases, putting it in a more competitive and favourable position to be the true phase. This work, in a way, established how metastable phase of a material could be stabilised through kinetics. It also opens a new dimension to the understanding of the phase diagram of Nitrogen under extreme conditions.

Finally, bimetallic Au_xAl_y clusters in which $x = y = n, 1 \leq n \leq 10$ were theoretically studied up to the bulk phase. The study reveals that each Au_nAl_n cluster adopt a geometric configuration that helps it to maximize the metal-metal interactions. It is further revealed that the four-member ring Au_2Al_2 cluster can be used as the building block to construct the other Au_nAl_n clusters up to the bulk (crystalline) phase. Since nanomaterial's properties depend on their size and shape, this study has presented a systemic approach to designing nanomaterials with specific physical (such as hardness) and chemical (such as catalytic) properties.

LIST OF REFERENCES

[1] R. Hoffman, Solids and surfaces: a chemist's view of bonding in extended structures. No. TR-39., (1988).

[2] B. M. Edward, F. C. Byrd, and W. D. Mattson. *High Energy Density Materials*. Springer Berlin Heidelberg 153 (2007).

[3] I. N. Levine, Quantum Chemistry. Englewood Cliffs, New jersey: Prentice Hall. pp. 455–544. *ISBN 0-205-12770-3* (1991).

[4] Acc. Chem. Res., **20** 134 (1987).

[5] B. Delley, "Modern density functional theory: a tool for chemistry, vol. 2 of theoretical and computational chemistry." *Elsevier Science Publ., Amsterdam* (1995).

[6] D. Sholl, and J. A. Steckel. *Density functional theory: a practical introduction*. John Wiley & Sons, (2011).

[7] P. Hohenberg and W. Kohn, Phys. Rev. **136**, B864 (1964).

[8] W. Kohn and L.J. Sham, Phys. Rev. **140**, A1133 (1965).

[9] L. H. Thomas, Proc. Camb. Philos. Soc. **23,** 542 (1927).

[10] J. C. Slater, Physical Review 81 3 **385** (1951).

[11] M. Born, and R. Oppenheimer, Annalen der Physik **389** 20 457 (1927).

[12] J. P. Perdew and A. Zunger, Phys. Rev. B **23**, 5048 (1981).

[13] D. M. Ceperley and B. J. Alder, Phys. Rev. Lett., **45**, 566 (1980).

[14] A. D. Becke, Phys. Rev. A **38** 3098 (1988).

[15] A. D. Becke, J. Chem. Phys. **88** 1053 (1988).

[16] K. Burke, J. P. Perdew, Y. Wang, Electronic Density Functional Theory. Springer US, 81 (1998).

[17] J. P. Perdew, K. Burke, M. Ernzerhof, Phys. Rev. Lett. ***77***, 3865 (1996).

[18] J. P. Perdew, Phys. Rev. Lett. **55**, 1665 (1985).

[19] J. P. Perdew, J. A. Chevary, S. H. Vosko, K. A. Jackson, M. Pederson, D. J. Singh, C. Fiolhais, Phys. Rev. B **46**, 6671 (1992).

[20] J. S. Tse, Y. Yao, D. D. Klug, S. Desgreniers, J. Phys. Conf. Series **121**, 012006 (2008).

[21] W. J. Evans, M. J. Lipp, C. S. Yoo, H. Cynn, J. L. Herberg, R. S. Maxwell, and M. F. Nicol, *Chem. Mater.* **18**, 2520 (2006).

[22] T. L. Gilbert, Phys. Rev. B **12**, 2111 (1975).

[23] H. J.Monkhorst and J. D. Pack, Phys. Rev. B **135**, 188 (1976).

[24] R. Orlando, R. Dovesi, C. Roetti, and V. R. Saunders, J. Phys. Condens. Matter **2**, 7769 (1990).

[25] V. R. Saunders, R. Dovesi, C. Roetti, M. Causà, N. M. Harrison, R. Orlando, and C. M. Zicovich-Wilson, CRYSTAL'98 User's Manual (University of Torino, Torino) (2003).

[26] J. M. Soler, E. Artacho, J. D. Gale, A. Garcia, J. Junquera, P. Ordejon, and D. Sanchez-Portal, J. Phys. Cond. Matt. **14**, 2745 (2002).

[27] J. C. Phillips, Phys. Rev. **112**, 685 (1958).

[28 J. C. Phillips and L. Kleinman, Phys. Rev. **116**, 287 (1959).

[29] M. L. Cohen and V. Heine, Solid State Physics **24**, 37 (1970).

[30] J. S. Lin, A. Qteish, M. C. Payne, and V. Heine. Phys. Rev. B **47**, 4174 (1993).

[31] This figure is taken from Yansun Yao's PhD Thesis (Department of Physics and Engineering Physics, University of Saskatchewan, 2008).

[32] S. Baroni, S. de Gironcoli, A. D. Corso, P. Giannozzi, Rev. Mod. Phys. **73**, 515 (2001).

[33] S. M. Mikki, A. K. Ahmed, "Particle swarm optimization: A physics-based approach." *Synthesis lectures on computational electromagnetics* **3** 1 (2008).

[34] M. J. Greschner, D. D. Klug, and Y. Yao. Phys. Rev. B **93**, 094428 (2016).

[35] H. Hellmann, Einfu¨hrung in die Quantenchemie (Deuticke, Leipzig) (1939).

[36] R. P. Feynman, Phys. Rev. **56**, 340 (1939).

[37] B. Kouchmeshky, N. Zabaras. Computational Materials Science **47**, 2, 342, (2009).

[38] I. Errea, M. Calandra, C. J. Pickard, J. Nelson, R. J. Needs, Y. Li, H. Liu, Y. Zhang, Y. Ma, F. Mauri. Phys. Rev. Lett. **114**, 157004 (2015).

[39] J. S. Tse, D. D. Klug, Y. Yao, Y. Le Page and J. R. Rodgers, Solid State Comm. **145**, 5 (2007).

[40] Q.Li , Z. Y. Jiang, M. Li, Y. Q.Hou, L. Si, X. D. Zhang, B. Zhou, Europhysics Letters, ***95*** 1 18002 (2011).

[41] G. Kresse, *Phys. Rev. B* **54**,11, 169 (1996).

[42] Togo, A. "Phonopy." (2014).

[43] P.E. Blöchl, Phys. Rev. B **50**, 17953 (1994).; G. Kresse and D. Joubert, Phys. Rev. B **59**, 1758 (1999).

[44] Y. Wang, J. Lv, L. Zhu, Y. Ma, Comput. Phys. Commun. ***183*** 2063 (2012).

[45] M. S. José, A. Emilio, D. G. Julian, G. Alberto, J. Javier, O. Pablo, and S.-P. Daniel, *J.* Phys. Condens. Matter **14**, 2745 (2002).

[46] Quantum-ESPRESSO is a community project for high-quality quantum-simulation software, based on density functional theory, and coordinated by Paolo Giannozzi. See http://www.quantum-espresso.org and http://www.pwscf.org.

[47] X. Gonze, Computational Materials Science **25** 3 478 (2002).

[48] R. Martoňák, A. Laio, and M. Parrinello, Phys. Rev. Lett. **90**, 075503 (2003).

[49] R. F. W. Bader, Atoms in molecules. John Wiley & Sons Ltd, (1990).

[50] F. Cacace, G. de Petris, and A. Troiani, Science **295**, 480 (2002).

[51] K. O. Christe, W. W. Wilson, J. A. Sheehy, and J. A. Boatz, Angew. Chem., Int. Ed. **38**, 2004 (1999).

[52] M. Eremets, A. Gavriliuk, I. A. Trojan, D. A. Dzivenko, and R. Boehler, Nat. Mater. **3**, 558 (2004).

[53] D. Tomasino, M. Kim, J. Smith, and C.-S. Yoo, Phys. Rev. Lett. **113**, 205502 (2014).

[54] C. Mailhiot, L. H. Yang, and A. K. McMahan, Phys. Rev. B **46**, 14419 (1992).

[55] B. Hirshberg, R. B. Gerber, and R. I. Krylov, Nat. Chem. **6**, 52 (2014).

[56] M. J. Greschner, M. Zhang, A. Majumdar, H. Liu, F. Peng, J. S. Tse, and Y. Yao, J. Phys. Chem. A **120**, 2920 (2016).

[57] W. D. Mattson, D. Sanchez-Portal, S. Chiesa, and R. M. Martin, Phys. Rev. Lett. **93**, 125501 (2004).

[58] M. M. G. Alemany and J. L. Martins, Phys. Rev. B **68**, 024110 (2003).

[59] F. Zahariev, J. Hooper, S. Alavi, F. Zhang, and T. K. Woo, Phys. Rev. B **75**, 140101 (2007).

[60] F. Zahariev, S.V. Dudiy, J. Hooper, F. Zhang, and T. K. Woo, Phys. Rev. Lett. **97**, 155503 (2006).

[61] X. Wang, Y. Wang, M. Miao, X. Zhong, J. Lv, T. Cui, J. Li, L. Chen, C. J. Pickard, and Y. Ma, Phys. Rev. Lett. **109**, 175502 (2012).

[62] C. J. Pickard and R. J. Needs, Phys. Rev. Lett. **102**, 125702 (2009).

[63] Y. Ma, A. R. Oganov, Z. Li, Y. Xie, and J. Kotakoski, Phys. Rev. Lett. **102**, 065501 (2009).

[64] J. Sun, M. Martinez-Canales, D. D. Klug, C. J. Pickard, and R. J. Needs, Phys. Rev. Lett. **111**, 175502 (2013).

[65] A. F. Goncharov, E. Gregoryanz, H. K. Mao, Z. Liu, and R. J. Hemley, Phys. Rev. Lett. **85**, 1262 (2000).

[66] E. Gregoryanz, A. F. Goncharov, R. J. Hemley, and H.-K. Mao, Phys. Rev. B **64**, 052103 (2001).

[67] M. I. Eremets, R. J. Hemley, H. K. Mao, and E. Gregoryanz, Nature **411**, 170 (2001).

[68] M. J. Lipp, J. P. Klepeis, B. J. Baer, H. Cynn,W. J. Evans, V. Iota, and C.-S. Yoo, Phys. Rev. B **76**, 014113 (2007).

[69] E. Gregoryanz, A. F. Goncharov, C. Sanloup, M. Somayazulu, H.-K. Mao, and R. J. Hemley, J. Chem. Phys. **126**, 184505 (2007).

[70] I. A. Trojan, M. I. Eremets, S. A. Medvedev, A. G. Gavriliuk, and V. B. Prakapenka, Appl. Phys. Lett. **93**, 091907 (2008).

[71] Y. Wang, J. Lv, L. Zhu, and Y. Ma, Phys. Rev. B: Condens. Matter Mater. **82**, 094116 (2010).

[72] P. Pavone, S. Baroni, and S. de Gironcoli, Phys. Rev. B **57**, 10421 (1998).

[73] S. Maintz, V. L. Deringer, A. L. Tchougréeff, and R. Dronskowski, J. Comput. Chem. **37**, 1030 (2016).

[74] R. Dronskowski and P. E. Bloechl, J. Phys. Chem. **97**, 8617 (1993).

[75] V. L. Deringer, A. L. Tchougréeff, R. Dronskowski, J. Phys. Chem. A **115**, 5461 (2011).

[76] A. R. Oganov and C. W. Glass, J. Chem. Phys. **124**, 244704 (2006).

[77] Y. Yao, J. S. Tse, and K. Tanaka, Phys. Rev. B **77**, 052103 (2008).

[78] A. H. Cowley, D. J. Mitchell, M. H. Whangbo, and S. Wolfe, J. Am. Chem. Soc. **101**, 5224 (1979).

[79] Y. Yao, R. Martoňák, S. Patchkovskii, and D. D. Klug, Phys. Rev. B **82**, 094107 (2010).

[80] H. W. Kroto, J. R. Heath, S. C. O'Brien, R. F. Curl, R. E. Smalley, Nature ***318***, 162 (1985).

[81] P. Pyykkö, Chem. Soc. Rev., ***37***, 1967 (2008).

[82] L. M. Wang, L. S. Wang, Nanoscale, ***4*** 4038 (2012).

[83] H. Häkkinen, R. N. Barnett, A. G. Scherbakov, U. Landman, J. Phys. Chem. B ***104***, 9063 (2000).

[84] J. Wang, G. Wang, G, J. Zhao, J. Phys. Rev. *B* ***66*** 035418 (2002).

[85] H. Häkkinen, B. Yoon, U. Landman, X. Li, H. J. Zhai, L. S. Wang, J. Phys. Chem. A ***107*** 6168 (2003).

[86] P. Pyykkö, Angew. Chem. Int. Ed. ***43*** 4412 (2004) ; W. Fa, C. Luo, J. Dong, Phys. Rev. B ***72***, 205428 (2005).

[87] C. Luo, W. Fa, J. Dong, J. Chem. Phys. ***125*** 084707 (2006).

[88] F. Remacle, E. S.Kryachko, J. Chem. Phys. ***122*** 044304 (2005).

[89] R. M. Olson, S. Varganov, M. S. Gordon, H. Metiu, S. Chretien, P. Piecuch, K. Kowalski, S. A. Kucharski, J. Am. Chem. Soc. ***127*** 1049 (2005).

[90] A. V. Walker, J. Chem. Phys. ***122*** 094310 (2005).

[91] Y. K. Han, J. Chem. Phys. ***124*** 024316 (2006).

[92] F. Wei, J. Dong, J. Chem. Phys. ***124*** 114310 (2006).

[93] J. Wang, H. Ning, Q. M. Ma, Y. Liu, Y. C. Li, J. Chem. Phys. ***129*** 134705 (2008).

[94] H. Häkkinen, Chem. Soc. Rev. ***37*** 1847 (2008).

[95] W. Huang, L. S. Wang, Phys. Rev. Lett. ***102***, 153401 (2009).

[96] X. Gu, M. Ji, S. H. Wei, X. G. Gong, Phys. Rev. B ***70*** 205401 (2004).

[97] P. Schwerdtfeger, Angew. Chemie Int. Ed. ***42*** 1892 (2003).

[98] P. Gruene, D. M. Rayner, B. Redlich, A. F. G. van der Meer, J. T. Lyon, G. Meijer, Science ***321***, 674 (2008).

[99] J. Li, X. Li, H. J. Zhai, L. S. Wang, Science, ***299*** 864 (2003).

[100] M. Ji, X. Gu, X. Li, J. Li, L. S. Wang, Angew. Chem. Int. Ed. ***44*** 7119 (2005).

[101] M. P. Johansson, D. Sundholm, J. Vaara, Angew. Chem. Int. Ed. ***43*** 2678 (2004).

[102] S. Bulusu, X. Li, L. S. Wang, X. C. Zeng, Proc. Natl. Acad Sci. *USA* ***103*** 8326 (2006).

[103] P. Pyykkö, Angew. Chem. Int. Ed. ***41*** 3573 (2002).

[104] D. E. Bergeron, A. W. Castleman Jr., T. Morisato, S. N. Khanna, J Chem. Phys. ***121*** 10456 (2004).

[105] C. Ashman, S. N. Khanna, F. Liu, P. Jena, T. Kaplan, M. Mostoller, Phys. Rev. B ***55*** 15868 (1997).

[106] J. U. Reveles, S. N. Khanna, P. J. Roach, A. W. Castleman, Proc. Natl. Acad. Sci. ***103*** 18405 (2006).

[107] D. E. Bergeron, A. W. Castleman Jr., T. Morisato, S. N. Khanna, Science ***304***, 84 (2004).

[108] D. E. Bergeron, P. J. Roach, A. W. Castleman Jr. N. O. Jones, S. N. Khanna, Science, ***307*** 231 (2005).

[109] M. Zhang, S. B. Yang, X. J. Feng, L. X. Zhao, H. Y. Zhang, Y. H. Luo, Eur. Phys. J. D ***67*** 1 (2013).

[110] Y. F. Li, Y. Li, X. Y. Kuang, Eur. Phys. J. *D*, ***67*** 1 (2013).

[111] C. Majumder, A. K. Kandalam, P. Jena, Phys. Rev. B ***74*** 205437 (2006).

[112] V. Kumar, Phys. Rev. B ***79*** 085423 (2009).

[113] M. Zhang, S. Chen, Q. M. Deng, L. M. He, L. N. Zhao, Y. H. Luo, Eur. Phys. J. D ***58***, 117 (2010).

[114] K. A. Gingerich, G. D. Blue, J. Chem. Phys. ***59*** 185 (1973).

[115] M. F. Cai, T. P. Dzugan, V. E. Bondybey, Chem. Phys. Lett. ***155*** 430 (1989).

[116] Z. Fu, G. W. Lemire, G. A. Bishea, M. D. Morse, J. Chem. Phys. ***93*** 8420 (1990).

[117] G. V. Lopez, J. Czekner, T. Jian, W. L. Li, Z. Yang, L. S. Wang, J. Chem. Phys. ***141*** 224309 (2014).

[118] N. S. Khetrapal,; T. Jian, R. Pal, G. V. Lopez, S. Pande,L. S. Wang, X. C. Zeng, Nanoscale ***8*** 9805 (2016).

[119] Y. Wang, M. Miao, J. Lv, L. Zhu, K. Yin, H. Liu, Y. Ma, J. Chem. Phys. ***137*** 224108 (2012).

[120] J. Lv, Y. Wang, L. Zhu, Y. Ma, J. Chem. Phys. ***137*** 084104 (2012**)**.

[121] B. Delley, J. Chem. Phys. ***92*** 508 (1990).

[122] J. P. Perdew, K. Burke, M. Ernzerhof, M. Phys. Rev. Lett. ***77*** 3865 (1996).

[123] S. J. Clark, M. D. Segall, C. J. Pickard, P. J.; Hasnip, M. I. J. Probert, K. Refson, M. C. Payne, Z. Kristallogr. ***220*** 567 (2005).

[124] S. Grimme, J. Comput. Chem. ***27*** 1787 (2006).

[125] G. Kresse, J. Hafner, Phys. Rev. B: Condens. Matter Mater. Phys. **47** 558 (1993).

[126] X. Wang, A. A. Adeleke, W. Cao, Y. Luo, M. Zhang, Y. Yao, J. Phys. Chem. C, ***120*** 25588 (2016).

[127] Z. H. Li, A. W. Jasper, D. G. Truhlar, J. Am. Chem. Soc. ***129*** 14899 (2007).

[128] A. Aguado, J. M. López, J. Chem. Phys. **130** 064704 (2009).

[129] F. Chuang, C. Z. Wang, K. H. Ho, Phys. Rev. B ***73*** 125431 (2006).

[130] J. U. Reveles, P. A. Clayborne, A. C. Reber, S. N. Khanna, K. Pradhan, P. Sen, M. R. Pederson, Nat. Chem. ***1***, 310 (2009)

[131] A. W. Castleman Jr., S. N. Khanna, J. Phys. Chem. C, ***113*** 2664 (2009).

[132] M. Zhang, J. Zhang, X. Feng, H. Zhang, L. Zhao, Y. Luo, W. Cao, J. Phys. Chem. A ***117*** 13025 (2013).

[133] X. Li, B. Kiran, J. Li, H. J. Zhai, L. S. Wang, Angewandte Chemie, ***114*** 4980 (2002).

[134] P. Pyykkö, N. Runeberg, Angewandte Chemie, ***114*** 2278 (2002).

[135] J. L. Murray, H. Okamoto, T. B. Massalski, Bulletin of Alloy Phase Diagrams, ***8***, 20 (1987).

[136] Z. Arunsingh, O. N. Srivastava, B. Dayal, Metallkd. ***61*** 383 (1970).

APPENDIX

PERMISSIONS

Chapter 3 is adapted with permission from Wang, X., Adeleke, A. A., Cao, W., Luo, Y., Zhang, M., & Yao, Y. Structures of Nanoalloy Clusters AunAln (n= 1–10) and the Growth Patterns to the Bulk Phase. J. Phys. Chem. C, **2016**, 120(44), 25588-25595. Copyright 2016 American Chemical Society (See below).

Figure 1.4. is reprinted with permission from Greschner, M. J., Klug, D. D., & Yao, Y., Phys. Rev. B 93, 094428 2016. Copyright 2016 by the American Physical Society (see below).

AMERICAN PHYSICAL SOCIETY LICENSE
TERMS AND CONDITIONS
Oct 16, 2017

This Agreement between Mr. Adebayo Adebayo ("You") and American Physical Society ("American Physical Society") consists of your license details and the terms and conditions provided by American Physical Society and Copyright Clearance Center.

License Number	4210911208972
License date	Oct 16, 2017
Licensed Content Publisher	American Physical Society
Licensed Content Publication	Physical Review B
Licensed Content Title	Prediction of a stable half-metal ferromagnetic BaCl solid
Licensed Content Author	Michael J. Greschner, Dennis D. Klug, and Yansun Yao
Licensed Content Date	Mar 24, 2016
Licensed Content Volume	93
Type of Use	Thesis/Dissertation
Requestor type	Student
Format	Print, Electronic
Portion	chart/graph/table/figure
Number of charts/graphs/tables/figures	1
Portion description	Figure 1: Pressure dependences of enthalpies for different structures, with the B1 structure as the zero-enthalpy reference.
Rights for	Main product
Duration of use	Life of Current Edition
Creation of copies for the disabled	yes
With minor editing privileges	no
For distribution to	Worldwide
In the following language(s)	Original language of publication
With incidental promotional use	no
The lifetime unit quantity of new product	0 to 499
The requesting person/organization is:	Adebayo Abayomi Adeleke
Order reference number	
Title of your thesis / dissertation	THEORETICAL PREDICTION AND STUDIES OF SELECTED NOVEL MATERIALS UNDER AMBIENT AND EXTREME CONDITIONS

Expected completion date	Dec 2017
Expected size (number of pages)	120
Requestor Location	Mr. Adebayo Adebayo 1217, 15th St. E Saskatoon, SK S7N 0R6 Canada Attn: Mr. Adebayo Adebayo
Billing Type	Invoice
Billing Address	Mr. Adebayo Adebayo 1217, 15th St. E Saskatoon, SK S7N 0R6 Canada Attn: Mr. Adebayo Adebayo
Total	0.00 USD

Terms and Conditions

Terms and Conditions

The American Physical Society (APS) is pleased to grant the Requestor of this license a non-exclusive, non-transferable permission, limited to [**print** and/or **electronic** format, depending on what they chose], provided all criteria outlined below are followed.

1. You must also obtain permission from at least one of the lead authors for each separate work, if you haven't done so already. The author's name and affiliation can be found on the first page of the published Article.

2. For electronic format permissions, Requestor agrees to provide a hyperlink from the reprinted APS material using the source material's DOI on the web page where the work appears. The hyperlink should use the standard DOI resolution URL, http://dx.doi.org/{DOI}. The hyperlink may be embedded in the copyright credit line.

3. For print format permissions, Requestor agrees to print the required copyright credit line on the first page where the material appears: "Reprinted (abstract/excerpt/figure) with permission from [(FULL REFERENCE CITATION) as follows: Author's Names, APS Journal Title, Volume Number, Page Number and Year of Publication.] Copyright (YEAR) by the American Physical Society."

4. Permission granted in this license is for a one-time use and does not include permission for any future editions, updates, databases, formats or other matters. Permission must be sought for any additional use.

5. Use of the material does not and must not imply any endorsement by APS.

6. Under no circumstance does APS purport or intend to grant permission to reuse materials to which it does not hold copyright. It is the requestors sole responsibility to ensure the licensed material is original to APS and does not contain the copyright of another entity, and that the copyright notice of the figure, photograph, cover or table does not indicate that it was reprinted by APS, with permission from another source.

7. The permission granted herein is personal to the Requestor for the use specified and is not transferable or assignable without express written permission of APS. This license may not be amended except in writing by APS.

8. You may not alter, edit or modify the material in any manner.

9. You may translate the materials only when translation rights have been granted.

10. You may not use the material for promotional, sales, advertising or marketing purposes.

11. The foregoing license shall not take effect unless and until APS or its agent, Copyright Clearance Center (CCC), receives payment in full in accordance with CCC Billing and Payment Terms and Conditions, which are incorporated herein by reference.

12. Should the terms of this license be violated at any time, APS or CCC may revoke the license with no refund to you and seek relief to the fullest extent of the laws of the USA. Official written notice will be made using the contact information provided with the permission request. Failure to receive such notice will not nullify revocation of the permission.

13. APS reserves all rights not specifically granted herein.

14. This document, including the CCC Billing and Payment Terms and Conditions, shall be the entire agreement between the parties relating to the subject matter hereof.

Other Terms and Conditions Version 1.1

Questions? customercare@copyright.com or +1-855-239-3415 (toll free in the US) or +1-978-646-2777.

Part of figure 2.8. is reprinted with permission from D. Tomasino, M. Kim, J. Smith, and C.-S. Yoo, Phys. Rev. Lett. **113**, 205502 2014. Copyright 2016 by the American Physical Society (see below).

AMERICAN PHYSICAL SOCIETY LICENSE
TERMS AND CONDITIONS
Oct 17, 2017

This Agreement between Mr. Adebayo Adebayo ("You") and American Physical Society ("American Physical Society") consists of your license details and the terms and conditions provided by American Physical Society and Copyright Clearance Center.

License Number	4211431244629
License date	Oct 17, 2017
Licensed Content Publisher	American Physical Society
Licensed Content Publication	Physical Review Letters
Licensed Content Title	Pressure-Induced Symmetry-Lowering Transition in Dense Nitrogen to Layered Polymeric Nitrogen (LP-N) with Colossal Raman Intensity
Licensed Content Author	Dane Tomasino et al.
Licensed Content Date	Nov 12, 2014
Licensed Content Volume	113
Type of Use	Thesis/Dissertation
Requestor type	Student
Format	Print, Electronic
Portion	chart/graph/table/figure
Number of charts/graphs/tables/figures	1
Portion description	Figure 3
Rights for	Main product
Duration of use	Life of Current Edition
Creation of copies for the disabled	no
With minor editing privileges	no
For distribution to	Worldwide
In the following language(s)	Original language of publication
With incidental promotional use	no
The lifetime unit quantity of new product	0 to 499
The requesting person/organization is:	Adebayo Adeleke
Order reference number	
Title of your thesis / dissertation	THEORETICAL PREDICTION AND STUDIES OF SELECTED NOVEL MATERIALS UNDER AMBIENT AND EXTREME CONDITIONS

Expected completion date	Dec 2017
Expected size (number of pages)	120
Requestor Location	Mr. Adebayo Adebayo 1217, 15th St. E Saskatoon, SK S7N 0R6 Canada Attn: Mr. Adebayo Adebayo
Billing Type	Invoice
Billing Address	Mr. Adebayo Adebayo 1217, 15th St. E Saskatoon, SK S7N 0R6 Canada Attn: Mr. Adebayo Adebayo
Total	0.00 USD

Terms and Conditions

Terms and Conditions

The American Physical Society (APS) is pleased to grant the Requestor of this license a non-exclusive, non-transferable permission, limited to [**print** and/or **electronic** format, depending on what they chose], provided all criteria outlined below are followed.

1. You must also obtain permission from at least one of the lead authors for each separate work, if you haven't done so already. The author's name and affiliation can be found on the first page of the published Article.

2. For electronic format permissions, Requestor agrees to provide a hyperlink from the reprinted APS material using the source material's DOI on the web page where the work appears. The hyperlink should use the standard DOI resolution URL, http://dx.doi.org/{DOI}. The hyperlink may be embedded in the copyright credit line.

3. For print format permissions, Requestor agrees to print the required copyright credit line on the first page where the material appears: "Reprinted (abstract/excerpt/figure) with permission from [(FULL REFERENCE CITATION) as follows: Author's Names, APS Journal Title, Volume Number, Page Number and Year of Publication.] Copyright (YEAR) by the American Physical Society."

4. Permission granted in this license is for a one-time use and does not include permission for any future editions, updates, databases, formats or other matters. Permission must be sought for any additional use.

5. Use of the material does not and must not imply any endorsement by APS.

6. Under no circumstance does APS purport or intend to grant permission to reuse materials to which it does not hold copyright. It is the requestors sole responsibility to ensure the licensed material is original to APS and does not contain the copyright of another entity, and that the copyright notice of the figure, photograph, cover or table does not indicate that it was reprinted by APS, with permission from another source.

7. The permission granted herein is personal to the Requestor for the use specified and is not transferable or assignable without express written permission of APS. This license may not be amended except in writing by APS.

8. You may not alter, edit or modify the material in any manner.

9. You may translate the materials only when translation rights have been granted.

10. You may not use the material for promotional, sales, advertising or marketing purposes.

11. The foregoing license shall not take effect unless and until APS or its agent, Copyright Clearance Center (CCC), receives payment in full in accordance with CCC Billing and Payment Terms and Conditions, which are incorporated herein by reference.

12. Should the terms of this license be violated at any time, APS or CCC may revoke the license with no refund to you and seek relief to the fullest extent of the laws of the USA. Official written notice will be made using the contact information provided with the permission request. Failure to receive such notice will not nullify revocation of the permission.

13. APS reserves all rights not specifically granted herein.

14. This document, including the CCC Billing and Payment Terms and Conditions, shall be the entire agreement between the parties relating to the subject matter hereof.

Other Terms and Conditions

Version 1.1

Questions? customercare@copyright.com or +1-855-239-3415 (toll free in the US) or +1-978-646-2777.